Nano Research

ISSN 1998-0124 CN 11-5974/O4
https://doi.org/10.26599/NR.2026.94909250

Research Article

Architecting honeycomb-like multistage structures via dual-powder alternately deposition additive manufacturing for enhanced FeCoNi soft magnetic alloys

Hui Xue[1](✉), Jianda Chen[1,2,4](✉), Shuai Hu[3,4], Ping Wang[3,4], Zhengyang Yu[1], Lei Wang[2], Delin Zhang[3,4], Yong Jiang[3,4](✉)

[1] School of Mechanical Engineering, Tiangong University, Tianjin 300387, China

[2] School of Materials Science and Engineering, Tiangong University, Tianjin 300387, China

[3] School of Electronic and Information Engineering, Tiangong University, Tianjin 300387, China

[4] Institute of Quantum Materials and Devices, Tiangong University, Tianjin 300387, China

Nano Res., **Just Accepted Manuscript** • https://doi.org/10.26599/NR.2026.94909250

https://www.sciopen.com/journal/1998-0124 on Oct. 12, 2026

© The Authors(s)

Just Accepted

This is a "Just Accepted" manuscript, which has been examined by the peer-review process and has been accepted for publication. A "Just Accepted" manuscript is published online shortly after its acceptance,which is prior to technical editing and formatting and author proofing. Tsinghua University Press (TUP) provides "Just Accepted" as an optional and free service which allows authors to make their results available to the research community as soon as possible after acceptance. After a manuscript has been technically edited and formatted, and the page proofs have been corrected, it will be removed from the "Just Accepted" web site and published officially with volume and article number (e.g., *Nano Research*, **2025**, *18*, 94906990). Please note that technical editing may introduce minor changes to the manuscript text and/or graphics which may affect the content, and all legal disclaimers that apply to the journal pertain. In no event shall TUP be held responsible for errors or consequences arising from the use of any information contained in these "Just Accepted" manuscripts. To cite this anuscript please use its Digital Object Identifier (DOI®),which is identical for all formats of publication.

Just Accepted

Research Article

Architecting honeycomb-like multistage structures via dual-powder alternately deposition additive manufacturing for enhanced FeCoNi soft magnetic alloys

Hui Xue [1,*], Jianda Chen [1, 2, 4, *], Shuai Hu [3,4], Ping Wang [3,4], Zhengyang Yu [1], Lei Wang [2], Delin Zhang [3,4], Yong Jiang [3,4,*]

[1] School of Mechanical Engineering, Tiangong University, Tianjin 300387, China

[2] School of Materials Science and Engineering, Tiangong University, Tianjin 300387, China

[3] School of Electronic and Information Engineering, Tiangong University, Tianjin 300387, China

[4] Institute of Quantum Materials and Devices, Tiangong University, Tianjin 300387, China

Received: 5 July 2026; **Revised:** 3 October 2026; **Accepted:** 12 October 2026

✉Address correspondence to Hui Xue, xuehui@tiangong.edu.cn; Jianda Chen, 18622511438@163.com; Yong Jiang, yjiang@tiangong.edu.cn

Cite this article: *Nano Research*, 2026, 19, 94909250 https://doi.org/10.26599/NR.2026.94909250

Just Accepted

Abstract: Soft magnetic materials are vital for a wide range of technologies. However, the very diversity of these applications poses a fundamental challenge for their design and manufacturing. This is compounded by a typical trade-off: improvements in mechanical property often necessitate a sacrifice in magnetic property, thus hindering the achievement of a comprehensive performance balance. To overcome this, we present a FeCoNi-based multi-principal element alloy fabricated via dual-powder alternately deposition additive manufacturing (AMed-AD). This approach creates a unique honeycomb-like multistage microstructure with coherent $(Fe, Co, Ni)_3Al$ precipitates. Compared with cast counterparts, the AMed-AD alloy achieves superior tensile strength (528.4 MPa) and elongation (35.4%)—improvements of 150% and 179%, respectively—while preserving magnetic properties due to the refined, homogeneous microstructure that minimizes domain-wall pinning. Corrosion resistance is also enhanced through microstructural refinement and chemical homogeneity. DFT calculations reveal that alloying increases charge localization and interfacial bonding while reducing the density of states at the Fermi level, collectively underpinning the improved mechanical, magnetic, and anti-corrosion performance. This work offers a microstructural engineering strategy to break traditional property trade-offs in soft magnetic alloys.

Keywords: Soft magnetic; Additive Manufacturing; Multi-principal element alloy; Alternately deposition; Multistage microstructure

Just Accepted

1. Introduction

Soft magnetic alloys are an important category of functional materials, featuring high magnetic permeability, low coercivity and low energy loss [1]. Owing to their superior magnetization and demagnetization behaviors, they have been widely applied in electromagnetic devices such as transformers, motors and sensors [2, 3]. Nevertheless, conventional soft magnetic alloys including Fe-Co [4], Fe-Si [5, 6] and Permalloy [7, 8] suffer from unsatisfactory mechanical properties [9]. It remains challenging for these materials to simultaneously achieve high strength, good ductility and desirable magnetic performance [10, 11].

Traditional methods to synthesize soft magnetic alloys, such as vacuum arc melting [12-14] and powder metallurgy [15, 16], inevitably introduce a large number of shrinkage cavities and notable compositional segregation within the as-prepared materials [17]. These structural defects severely degrade the mechanical performance, manifesting as low strength and limited plastic deformability. Direct energy deposition (DED) is an additive manufacturing (AM) technology that constructs intricate 3D structures through melting feedstock metal powders or wires using high-energy heat sources [18-20]. Characterized by ultra-high cooling rates and steep thermal gradients, DED enables the formation of dense, fine-grained microstructures, thereby remarkably improving the mechanical properties of alloys [21]. Moreover, its advantages in high material efficiency and shortened production period render DED an ideal candidate for exploring new material systems and realizing rapid manufacturing. For these reasons, DED is regarded as a promising route to produce high-performance soft magnetic materials.

The equiatomic FeCoNi alloy possesses a single-phase face-centered cubic (FCC) crystal structure, endowing it with prominent magnetic properties including high

Just Accepted

saturation magnetization (Ms), a high Curie temperature, and relatively low coercivity [22]. Despite these advantages, its mechanical performance is rather deficient, which restricts its practical application in high-load-bearing scenarios that demand superior strength. To address this critical issue, researchers have devoted considerable attention to the equiatomic FeCoNi alloy in recent years, developing a series of multi-principal element alloys through the precise and strategic control of alloying compositions. Notably, this design approach has achieved the synergistic enhancement of magnetic performance and mechanical properties, overcoming the traditional trade-off between these two functionalities. An in-situ TiC-reinforced metastable composite, fabricated via mechanical alloying combined with spark plasma sintering [23], achieved a yield strength of 910 MPa, an elongation of 10.9%, a Ms of 141 emu/g, and a coercivity (Hc) of 7.74 Oe. For the $(FeCoNi)_{86}Al_4Cu_3Ti_7$ high-entropy alloy, prepared by vacuum arc melting followed by heat treatment [24], the corresponding properties were reported as 1287 MPa (yield strength), 15% (elongation), 100 emu/g (Ms), and 26.21 Oe (Hc). Similarly, the vacuum arc-melted $FeCoNi(MnAl)_{0.25}$ alloy [25] exhibited a yield strength of 331 MPa and 45% elongation after heat treatment; in the as-cast state, it retained favorable soft magnetic properties with an Ms of 101 emu/g and Hc of 3.35 Oe. Traditional alloy strengthening primarily relies on conventional manufacturing and post-treatment processes [26]. However, these techniques are inherently limited in their capacity to fabricate complex-shaped components or achieve precise control over microstructural features [27, 28].

To address the challenge that conventional FeCoNi soft magnetic alloys struggle to simultaneously achieve high strength, excellent ductility, and superior soft magnetic properties, this study first fabricated two types of FeCoNi soft magnetic alloys via casting and DED techniques, respectively, to clarify the process advantages

Just Accepted

of DED. Subsequently, using the equiatomic FeCoNi alloy as the matrix, two FeCoNi-based soft magnetic high-entropy alloy (HEA) systems were designed by incorporating 316L stainless steel (SS) as well as Ti, Al, and Nb elements, followed by their fabrication via DED. By systematically comparing the differences in microstructures and comprehensive properties between the two alloys, the influence mechanism of element addition on alloy microstructural evolution and performance regulation was thoroughly elucidated. On this basis, by alternately depositing two mixed powders, FeCoNi-$(Ti46Al7.7Nb)_{2at.\%}$ and FeCoNi-$(316L)_{5wt.\%}$, a FeCoNi-based soft magnetic HEA with a microscale alternately composite structure was successfully fabricated, which ultimately achieves synergistic improvements in both mechanical and soft magnetic properties on this basis.

2. Materials and methods

2.1 Preparation of pre-alloyed powders

Electrode Induction Gas Atomization (EIGA) was employed to produce alloy powders (50~150 μm) from starting ingots of FeCoNi, Ti46Al7.7Nb, and 316L SS. In this process, the billets are induction-melted within the atomization chamber, and the applied electrode current generates a plasma on the melt surface. A high-velocity argon stream is subsequently introduced through the plasma zone, whereupon the alloy rapidly expands, cools and solidifies into micrometer-sized particles. The particle morphology and size distribution of the as-synthesized FeCoNi powders are presented in **Figs. 1**(a-b), while the corresponding results for the Ti46Al7.7Nb and 316L SS powders are given in **Fig. S1**. Phase identification reveals that all three pre-alloyed powders consist predominantly of the γ phase, accompanied by a minor fraction of the α_2 phase (Fig. 1(c)).

The first type of mixed powder was prepared by ball milling FeCoNi and

Just Accepted

Ti46Al7.7Nb powders, and the second type of mixed powder was produced from FeCoNi and 316L SS powders using the same process. The ball milling process was conducted at 200 r/min for 480 minutes with a ball-to-powder ratio of 6:1. A schematic diagram of the milling setup is shown in Fig. 1(d). The mixed powder was finally dried in a vacuum oven at 150 ℃ for 24 h. A 304L SS substrate was selected, mechanically ground to remove the surface oxide layer and achieve a smooth finish, and subsequently cleaned ultrasonically.

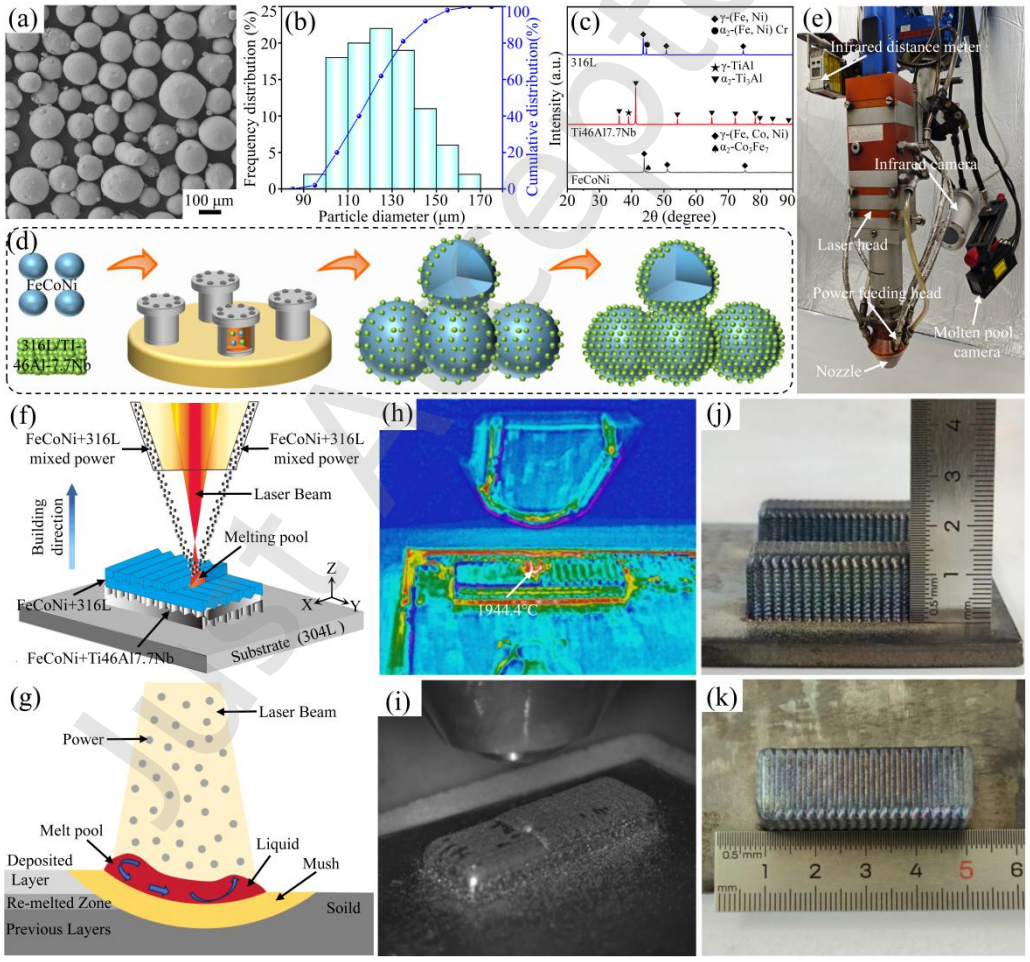


Figure 1 (a) The morphology of FeCoNi pre-alloy powders; (b) Grain size statistics; (c) XRD pattern of three kinds of powders; (d) Powder ball milling process; (e) Laser head; (f) Schematic illustration of the DED process; (g) Heat-affected zone of the molten; (h) Temperature variations during the deposition process; (i) Deposition

procedure under the molten pool camera; (j) The front view of the AMed-AD FeCoNi alloy; (k) Top view.

2.2 Sample fabrication and AM process

FeCoNi alloy was fabricated via vacuum arc melting (VAM) using high-purity Co, Ni, and Fe elements as raw materials (purity ≥ 99.9%). Prior to melting, the melting furnace was first evacuated to 5.0 Pa, followed by purging with argon gas. This evacuation-argon purging cycle was repeated at least twice to thoroughly remove residual air inside the furnace. Finally, after maintaining the vacuum degree of the furnace below 5×10^{-3} Pa, an appropriate amount of argon gas was introduced as a protective atmosphere to initiate the melting process. To ensure the uniformity of element distribution in the alloy, each alloy sample was remelted at least five times. After completion of melting, the molten alloy was poured into a suction casting mold with dimensions of 12 mm × 12 mm × 60 mm, and suction casting was carried out under the protection of high-purity argon gas.

The deposition was performed in an argon chamber using a DED system equipped with a fiber laser (Fig. 1(e)), employing a combined linear and cross-scanning strategy. Two layers of the first type of powder mixture were initially deposited. The powder feeder was then switched to deposit two layers of the second type of mixture on top. This alternately process was repeated to build up the structure, as illustrated in Fig. 1(f). As shown in the molten pool schematic (Fig. 1(g)), the previously deposited alloy is reheated, thereby subjecting it to an in-situ heat treatment. The process maintained stable deposition parameters throughout, ensuring uniform layer formation and enabling the fabrication of a fully dense FeCoNi-based soft magnetic multi-principal element alloy. Temperature evolution during deposition

Just Accepted

was recorded with an infrared thermal imager (Fig. 1(h)). A sharp temperature decrease was observed as the material moved away from the laser beam, demonstrating rapid solidification of the alloy. In-situ monitoring of the deposition process was performed with a molten pool camera (Fig. 1(i)), demonstrating that the molten pool possessed highly favorable flow characteristics.

To prevent molten pool oxidation during the DED process, the argon gas pressure was maintained constant, and the oxygen level was controlled below 50 ppm. Based on the research conducted on AM FeCoNi alloys [29, 30] and the actual adjustment of process parameters, definite process parameters: The depositioned layer thickness of 0.5 mm, coaxial powder feed rate of 2.3 g/min, laser power of 800 W, beam diameter of 2.2 mm, scanning speed of 6 mm/s, and overlap ratio of 50%. The deposit attained final dimensions of 40 mm × 12 mm × 13 mm (Figs. 1(j-k)). Its macroscopic morphology was characterized by a dense surface devoid of cracks and pores.

2.3 Performance testing

The sample was sectioned parallel to the building direction (BD) using wire electrical discharge machining. The magnetic hysteresis loop of the sample was measured using a vibrating sample magnetometer (VSM) under an applied field of ±10,000 Oe at a sweep rate of 140 Oe/s, with the field direction parallel to the sample surface. The Ms and Hc were determined from the obtained loop. Uniaxial tensile tests were conducted on an electronic universal testing machine at a strain rate of 1×10^{-2} s^{-1}, with the loading direction parallel to BD. A minimum of three specimens were tested under identical conditions, and the average values are reported.

The electrochemical corrosion behavior of the alloys was evaluated using a CHI-600 E electrochemical workstation with a three-electrode cell in a 3.5 wt.% NaCl solution at room temperature. The electrodes (CE), reference electrode (RE) and

Just Accepted

working electrode are respectively a Pt electrode, an AgCl electrode (SCE) and an alloy sample with dimensions of 10 mm × 10 mm × 1 mm. Before the electrochemical corrosion test, to obtain a stable open-circuit potential (OCP), immerse the sample in the electrolyte for 60 minutes. Within the corrosion potential range of -2 V to 2 V, measure the electromotive potential polarization curve at a scanning speed of 10 mV/s. Under the OCP constant potential condition, with a frequency range of 10^{-2} to 10^{-5} Hz and a voltage perturbation amplitude of 10 mV, the electrochemical impedance spectroscopy (EIS) was measured.

2.4 Microstructural characterization

Microstructural characterization was performed using scanning electron microscopy (SEM) in backscattered electron (BSE) mode at an accelerating voltage of 20 kV and a working distance of 8 mm. All specimens were prepared by standard mechanical polishing, achieving a final surface finish of 0.05 μm. Crystallographic characterization was performed using electron backscatter diffraction (EBSD) at an acceleration voltage of 20 kV with a step size of 2 μm. Data were processed using the HKL Channel 5 system (Oxford Instruments). Elemental mapping was carried out by electron probe microanalysis (EPMA). Perform X-ray diffraction (XRD) analysis using the Bruker D8 Advance device equipped with Cu-Kα diffraction. The operating voltage is 40 kV and 30 mA, scanning rate is 6° $minute^{-1}$, step size is 0.02°. The 2θ diffraction angle range is from 20° to 90°. Microstructural analysis was performed by transmission electron microscopy (TEM) at an accelerating voltage of 300 kV. Samples were firstly mechanically ground to approximately 60 μm, followed by electropolishing using a twin-jet system with an electrolyte of 65 vol% methanol, 30 vol% butanol, and 5 vol% perchloric acid at 30 V and –30 °C to electron transparency. Observing the macroscopic morphology of tensile fracture surfaces using a 3D

Just Accepted

Measuring Microscope.

2.5 Density functional theory calculation details

First-principles calculations in this work were performed using the Vienna ab initio simulation package (VASP) [31, 32]. The generalized gradient approximation by Perdew-Burke-Ernzerhof (PBE) was employed to describe the exchange-correlation functional [33]. The ion-electron interaction was estimated by the projector augmented wave model [34]. The k-point mesh for the surface slab model and the primitive cell were 3 × 3 × 1 and 7 × 7 × 7, respectively. Moreover, the energy cutoff for the plane wave expansion was set to 450 eV. The energy convergence for terminating the electronic self-consistent field was 10^{-6} eV/atom, and the force convergence on each atom for geometric optimization was 10^{-2} eV/Å.

3. Results and discussion

3.1 Microstructure characterization

To investigate the effects of two fabrication routes on the microstructures and properties of FeCoNi-based alloys, comparative microstructural characterizations were carried out on FeCoNi alloys fabricated via as-cast (AC) and additively manufactured (AMed) processes. The AC alloy exhibits coarse and irregular grains with typical microstructural features of high-temperature cast ingots. Distinct striped segregation bands can be observed inside grains (**Figs. 2**(a_1-a_2)). This segregation originates from the uneven flow of liquid metal during casting, which triggers compositional segregation and consequently leads to heterogeneous element distribution within the alloy matrix [35]. In addition, fine pore defects are dispersed throughout the alloy, which mainly result from volume shrinkage during solidification and incomplete gas evacuation.

In contrast, distinct fish-scale molten pool morphologies can be observed in the AMed alloy, with regularly semi-elliptical molten pool boundaries and satisfactory

Just Accepted

overall microstructural homogeneity (Figs. 2(b_1-b_2)). This characteristic is primarily attributed to the relatively simple composition and low melting point of the alloy, which endow the molten pool with favorable fluidity and thermal conductivity and thus produce relatively large molten pools. During solidification, grains show an obvious coarsening tendency, and columnar grains epitaxially grow perpendicular to the molten pool boundaries, delivering excellent microstructural continuity yet limited grain refinement effect.

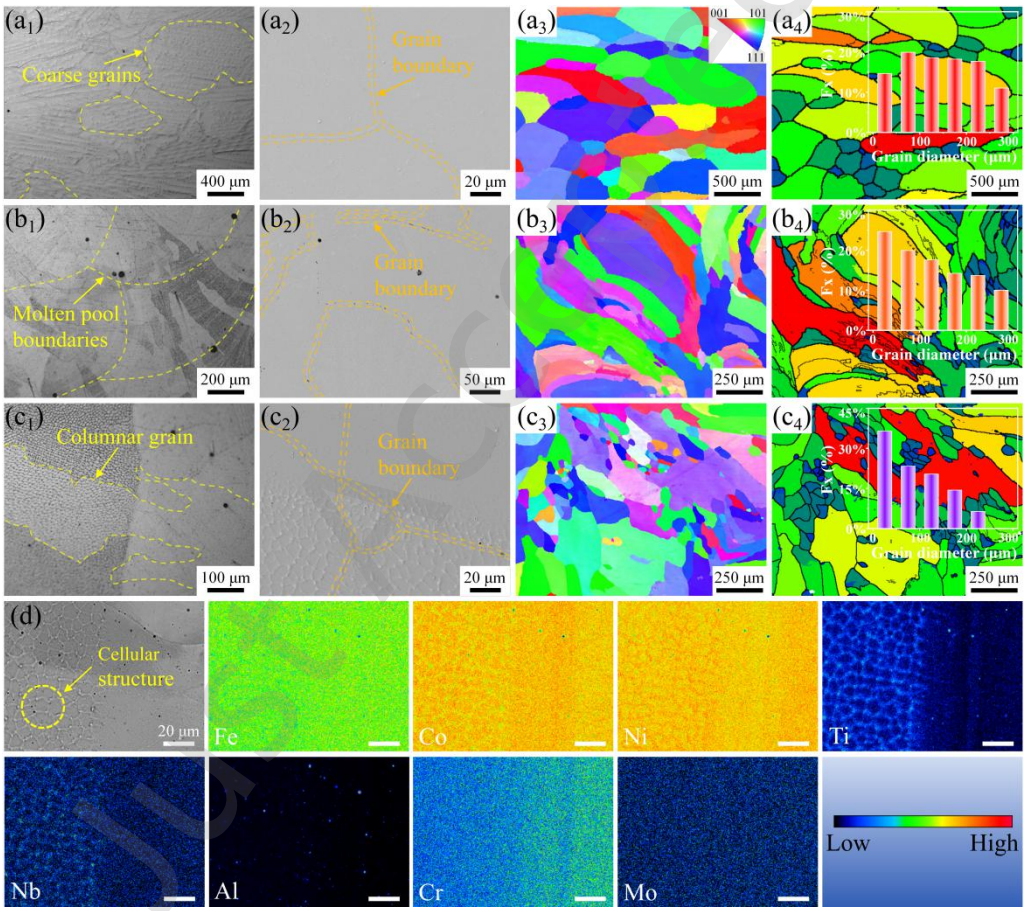


Figure 2 Microstructures for the AC/AMed/AMed-AD FeCoNi alloy: (a–c) OM/SEM/EBSD images, grain boundary distribution and grain size distribution images; (d) SEM-BSE and corresponding EPMA characterizations of the AMed-AD FeCoNi alloy.

To explore the influence of compositional modulation on the microstructural

evolution of DED-fabricated FeCoNi-based soft magnetic HEA, microstructural characterizations are analyzed in detail, with detailed descriptions provided in the **Supplementary Materials**. The metallographic microstructure of AMed-AD is displayed in **Figs.** 2(c_1) and **S3**. Periodically distributed alternating light and dark layered structures with uniform layer thickness and distinct periodicity can be clearly observed in the alloy. Specifically, the light-colored regions correspond to the deposited layers of FeCoNi-$(316L)_{5wt.\%}$, while the dark-colored regions represent the deposited layers of FeCoNi-$(Ti46Al7.7Nb)_{2at.\%}$. The interlayer interfaces exhibit dense and sound bonding, without obvious defects such as pores, cracks, or lack of fusion. No noticeable elemental segregation or excessively thick diffusion transition layers emerge at the interfaces, demonstrating the achievement of superior metallurgical bonding between heterogeneous materials via the DED process. This alternately composite microstructure, constructed by periodic compositional modulation, endows the alloy with distinctive structural features. It effectively tailors magnetic domain motion and mechanical deformation behavior, thereby laying a robust structural basis for the synergistic optimization of the alloy's soft magnetic and mechanical properties.

The SEM microstructure and corresponding local magnified images of the AMed-AD alloy are presented in Fig. 2(c_2). The characterization results reveal that the two types of composite powders are well composited after layer-by-layer deposition via the DED process. Columnar grains with a preferential growth direction emerge in the interlayer regions, which grow approximately perpendicular to the layer interfaces and exhibit typical directional solidification characteristics. The adjacent layers possess distinct interfaces and compact bonding, with no microcracks or lack-of-fusion defects detected, indicating favorable interlayer metallurgical bonding

Just Accepted

quality. A small number of micro-pores are observed in localized regions, which are speculated to be gas pores formed by the untimely escape of trapped gas during solidification. The overall microstructure is uniform and dense without evident microstructural inhomogeneity, verifying that the alternately deposition process effectively guarantees the structural stability and consistency of the alloy microstructure.

Figure 2(a_3) and (b_3) display the inverse pole figure (IPF) maps of AC and AMed alloys. In these maps, red, green, and blue colors correspond to grains with (001), (101), and (111) crystallographic orientations parallel to the sample normal (BD), respectively. A comparative analysis of the IPF maps of pristine FeCoNi alloys fabricated by the two processing methods indicates that the AC alloy exhibits a uniform distribution of red, green, and blue grains with a comparable area fraction for each grain orientation. This phenomenon suggests that the grain growth of the AC alloy is barely affected by directional heat flow or preferential growth mechanisms during solidification, presenting typical characteristics of random nucleation and grain growth[27]. In contrast, the AMed alloy contains coarse and irregularly shaped grains with subtle intragranular color variations, implying excellent orientation consistency within individual grains. Nevertheless, significant orientation discrepancies exist between adjacent grains.

Alloys prepared by the two processes both exhibit random orientation characteristics. Specifically, the AC alloy shows a more uniform distribution, whereas the AMed alloy has coherent intragranular orientations but pronounced intergranular divergence, presumably owing to the relatively simple FeCoNi composition. For the as-cast process, the slow solidification rate of liquid metal imposes negligible constraints on nucleation and grain growth, thereby resulting in completely random

Just Accepted

grain orientations. Although directional heat flux exists during the DED process, the simple composition of the FeCoNi alloy leads to a limited number of nucleation sites and low restriction on grain growth. Consequently, no intense directional solidification texture is formed, and only discrete orientation distribution among grains is observed[36, 37].

Compared with the AC alloy, all FeCoNi-based alloys fabricated via DED exhibit prominent grain refinement, which is primarily attributed to the unique high cooling and solidification rates of the DED process that effectively restrain grain growth [38]. In detail, the AMed alloy still presents the largest grain size with a relatively wide distribution range, mainly varying from 80 to 150 μm (Fig. 2(b_4)). This phenomenon is closely related to its relatively simple alloy composition. Limited nucleation sites are available during solidification, leading to a low degree of constraint on grain growth. Although the rapid solidification effect of DED refines the grains compared with the as-cast counterpart, the overall grain refinement effect is relatively limited.

After the addition of 5wt.% 316L SS, the alloy is markedly refined with a narrowed grain size distribution, and the average grain size is significantly reduced relative to the AMed alloy (Fig. S4(a_2)). By contrast, doping with Ti, Al and Nb produces the most pronounced grain refinement, further shifting the grains into a finer regime, with the majority below 50 μm (Fig. S4(b_2)). Overall, as the alloy composition becomes more complex, the grain size of DED-processed FeCoNi-based soft magnetic alloys exhibits a gradual declining trend and the microstructural homogeneity is continuously improved. The composite addition of Ti, Al, and Nb elements demonstrates the optimal modulation effect on grain refinement.

The IPF map of the AMed-AD alloy is displayed in Fig. 2(c_3), revealing a relatively uniform and random grain orientation distribution within the alloy. The red,

Just Accepted

green, and blue regions are homogeneously dispersed throughout the map with comparable area fractions, and no predominant crystallographic orientation is detected, indicating that no distinct directional solidification texture is formed in the overall alloy microstructure. Affected by the layered composition-modulated structure, the grain morphology exhibits distribution characteristics correlated with the compositional layers.

In some regions, grains are refined with diverse orientations, whereas adjacent regions contain relatively coarser grains that still retain a random orientation distribution. Minor intragranular color variations indicate good orientation coherence within individual grains, while neighboring grains exhibit pronounced orientation differences, reflecting large grain-boundary misorientation angles. These random orientations are attributed to the alternating solidification of the two constituent layers during deposition: such layered solidification interrupts the continuous epitaxial growth of columnar grains, thereby suppressing the development of a single preferred orientation.

The grain size distribution of the AMed-AD alloy, statistically derived from EBSD data, is shown in Fig. 2(c_4). Relative to the single-component alloys, the alternating composite alloy has a smaller average grain size than the FeCoNi-$(316L)_{5wt.\%}$ alloy, but is slightly coarser than the $(FeCoNi)Ti_2Al_2Nb_{0.33}$ alloy. Its relatively broad distribution, concentrated mainly in the 30~100 μm range, forms a distinct grain-size gradient.

This phenomenon is primarily attributed to the alternating solidification behavior between the two compositional layers during the alternately deposition process, where the grain refinement effects of the two alloys are mutually coupled. Meanwhile, the existence of interlayer interfaces effectively interrupts the continuous epitaxial growth

Just Accepted

of columnar grains and facilitates repeated nucleation and grain refinement. In addition, the periodic alternation of composition-modulated layers induces subtle differences in local grain growth conditions, resulting in slight fluctuations in grain size. Overall, the microstructure exhibits favorable homogeneity without the emergence of abnormally coarse grains.

EPMA was employed to characterize the microscale elemental distribution of the AC alloy and the AMed-AD alloy, and the corresponding results are presented in **Figs.** 2(d) and **S5**. The elemental distribution results indicate that the AC alloy achieves uniform elemental distribution (Fig. 2(d)). In comparison, obvious segregation of Co, Ni, Ti, and Nb occurs along the boundaries of cellular structures in the AMed-AD alloy, while Fe, Al, Cr, and Mo exhibit relatively homogeneous distribution characteristics. These results demonstrate that the formation of cellular structures is primarily attributed to the segregation behavior of Ti and Nb elements.

The formation of cellular or dendritic microstructures generally follows the solute redistribution mechanism during solidification. At the initial stage of solidification, solute atoms are rejected and enriched at the front of the solid–liquid interface, and are subsequently trapped in the intercellular or interdendritic regions, as well as at grain boundaries formed during the final solidification stage. Accordingly, the development of cellular structures originates from the significant atomic radius differences among alloying elements and their non-equilibrium partitioning behavior under rapid solidification conditions.

Specifically, Ti (170 pm) and Nb (173 pm) possess considerably larger atomic radii than the matrix elements of Fe (148 pm), Co (150 pm), and Ni (149 pm), whereas Al (143 pm), Cr (135 pm), and Mo (145 pm) have relatively smaller atomic radii. Under the unique rapid solidification conditions of the DED process, the

Just Accepted

diffusion of large-sized Ti and Nb atoms is restricted at the solid–liquid interface front. These atoms tend to be rejected and enriched ahead of the advancing solidification interface, eventually inducing distinct elemental segregation at the boundaries of cellular structures. In contrast, elements with smaller atomic radii (Fe, Al, Cr, and Mo) exhibit superior diffusion capability and achieve homogeneous redistribution at the solid–liquid interface [39-41].

Furthermore, the inherent non-equilibrium solidification characteristics of DED amplify the difference in effective solute partition coefficients between the liquid and solid phases, facilitating the microscopic elemental segregation between the interior and boundaries of cellular structures. Such solute redistribution behavior, jointly driven by the atomic size effect and rapid solidification kinetics, serves as the fundamental mechanism for the formation of cellular structures and their corresponding elemental distribution characteristics [42, 43].

Just Accepted

3.2 Phases composition

To further reveal the microstructural characteristics of AMed-AD alloy, TEM was utilized to conduct detailed characterizations of AC and AMed-AD alloy samples. The bright-field TEM morphology displayed in **Fig. 3**(a) demonstrates that a typical honeycomb cellular structure is formed within the composite alloy. High-magnification morphological observations confirm that numerous spherical nano-scale precipitated particles are densely and dispersively distributed in the alloy matrix, as illustrated in Fig. 3(b). Qualitative compositional detection of the precipitated phases was performed via microscale energy spectrum analysis. The results indicate that these nano-precipitated phases are rich in Fe, Co, Ni, and Al elements, which can be identified as $(Fe,Co,Ni)_3$ Al intermetallic compounds. The

corresponding elemental distribution and compositional analysis results are presented in Fig. 3(c).

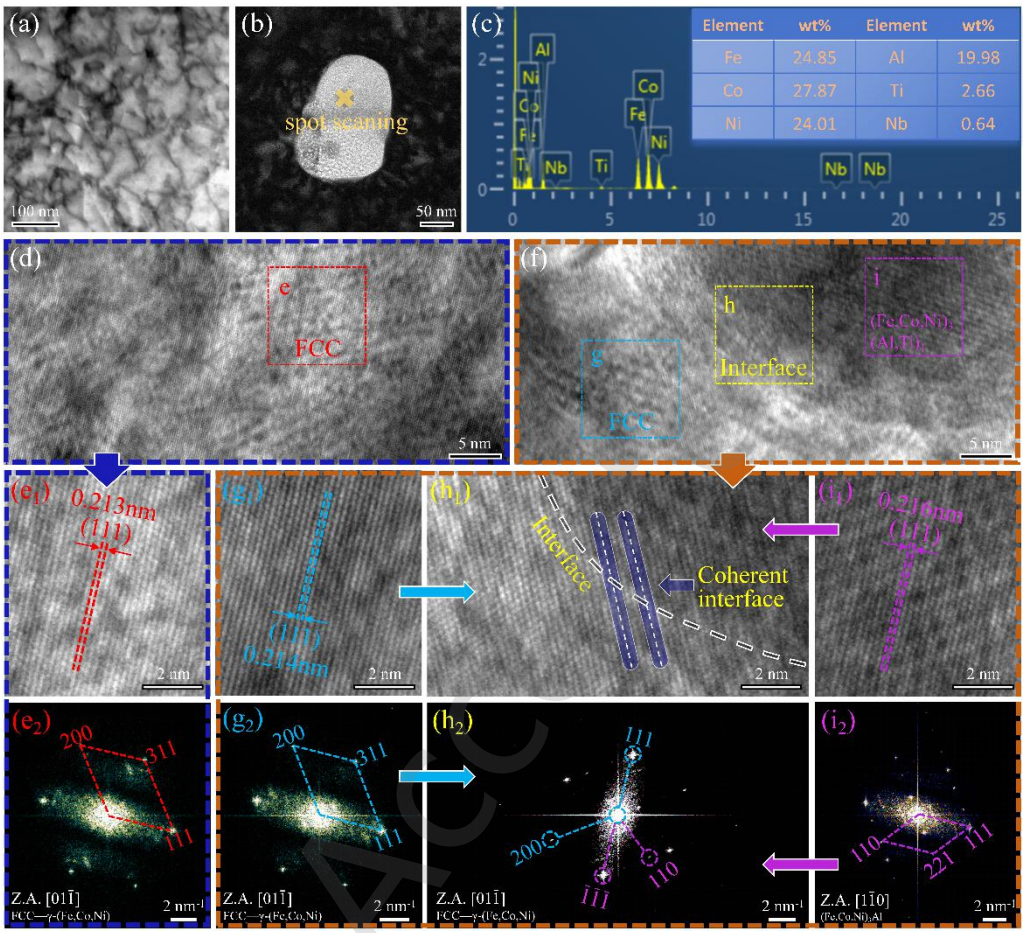


Figure 3 TEM images of the AMed-AD FeCoNi-based alloy: (a) Bright-field TEM images and the cellular structure; (b) Bright-field image of precipitates; (c) The distribution of elements in the precipitate; (d) Matrix of the alloy; (e_1-e_2) High-resolution image of region e in (d) and its SADP pattern; (f) The interfaces between the precipitates and matrix of the alloy; (g_1-g_2, h_1-h_2, i_1-i_2) High-resolution image of region g/h/i in (f) and its SADP pattern.

Figure 3(d) shows the bright-field TEM image of the AC alloy matrix, which exhibits a uniform single-phase microstructure throughout the alloy. A typical local region marked b was selected for high-resolution TEM analysis, and the

corresponding result is displayed in Fig. 3(e_1). Regularly arranged atomic-scale lattice fringes can be clearly observed within the field of view. Fast Fourier transform (FFT) was performed on this microregion to acquire the corresponding diffraction pattern, as presented in Fig. 3(e_2). Diffraction calibration results verify that the matrix of the AC alloy possesses a single-phase FCC structure, corresponding to the γ-(Fe,Co,Ni) solid solution. Accurate measurement yields an interplanar spacing of 0.213 nm for the (111) crystal plane, which is highly consistent with the standard theoretical parameters of the FCC-type γ-(Fe,Co,Ni) phase. This finding not only confirms the structural integrity of the matrix crystal structure but also demonstrates that alloying elements are fully dissolved into the matrix under as-cast conditions, without the precipitation of distinct secondary phases.

Figure 3(f) presents the bright-field TEM image of the AMed-AD alloy. The HRTEM morphologies of the matrix region, matrix/precipitate interface, and nano-sized precipitates are displayed in Figs. 3(g_1), (h_1), and (i_1), respectively. FFT analysis was conducted on the matrix microregion, and the corresponding result is shown in Fig. 3(g_2). The analytical results reveal that the composite alloy still maintains a stable FCC structure dominated by the γ-(Fe,Co,Ni) solid solution, despite the solid solution infiltration of Ti, Al, Nb, Cr, and Mo elements into the γ matrix under rapid solidification conditions. Compared with the AC alloy, the interplanar spacing of the (111) crystal plane of the composite alloy slightly increases to 0.214 nm, generating a minor lattice expansion of approximately 0.001 nm. This variation is primarily attributed to the occupation of lattice substitution sites by large-sized solute atoms such as Al and Ti, which induces local lattice distortion. Although a slight deviation in lattice parameters is observed, the measured values remain highly consistent with the standard theoretical data, demonstrating the overall

Just Accepted

structural stability of the matrix in the alternately deposited composite alloy. Furthermore, HRTEM characterization and FFT analysis of the nano-precipitates determine that the interplanar spacing of their characteristic crystal planes is 0.216 nm (Figs. 3(i_1–i_2)).

Notably, the interface region between the matrix and precipitates exhibits unique crystallographic characteristics, as displayed in Fig. 3(h_1). The lattice orientations of the matrix and precipitates on both sides of the interface are highly consistent, and continuous lattice fringes traverse the entire interface without obvious fracture or lattice misfit. This phenomenon directly demonstrates the existence of a specific crystallographic orientation relationship and favorable interfacial bonding between the two phases. FFT analysis was further performed on the interfacial microregion to obtain a composite diffraction pattern, as illustrated in Fig. 3(h_2). The characteristic diffraction spots of the matrix and precipitates are well matched and closely positioned, which further verifies that the two-phase interface possesses a coherent or semi-coherent structure. Such superior lattice matching can effectively reduce the interfacial energy and improve the structural stability of the microstructure.

Combined with the elemental ratios obtained from the preceding energy spectrum analysis and the crystallographic orientation characteristics revealed by high-resolution lattice characterization and FFT diffraction calibration, the nano-precipitated phase can be identified as the $(Fe,Co,Ni)_3Al$ intermetallic compound. A definite orientation correspondence is established between the precipitates and the matrix, namely (111)γ-(Fe,Co,Ni) ∥ (111)$(Fe,Co,Ni)_3$ Al. The coherent interface formed between the two phases significantly reduces the interfacial distortion energy, thereby providing favorable thermodynamic conditions for the uniform nucleation and stable growth of nano-precipitates. Ultimately, this effect

Just Accepted

enables the strengthening phases to achieve a stable and dispersed distribution within the alloy matrix.

3.3 Magnetic properties

Figures 4(a-b) presents the hysteresis loops and corresponding local enlarged views of FeCoNi-based soft magnetic alloys measured at room temperature. The test results show that the AC alloy exhibits a Ms of approximately 179.52 emu/g and a Hc of 3.17 Oe. By comparison, the AMed alloy possesses a Ms of around 179.89 emu/g and a Hc of 3.14 Oe. These results demonstrate that the DED technique exhibits unique advantages in regulating the soft magnetic properties of FeCoNi-based alloys. The superior magnetic properties of the DED-fabricated alloy are primarily attributed to its unique high solidification rate and thermal cycle characteristics. The distinctive rapid melting and solidification process of DED significantly restricts the macroscopic diffusion of elements, homogenizes the microstructural and compositional distribution of the alloy, and eliminates the macroscopic segregation commonly observed in traditional casting processes, thereby optimizing the uniformity and stability of magnetic performance. Furthermore, the layer-by-layer deposition mode is accompanied by a repeated cyclic heat treatment effect, which promotes the rearrangement of dislocation structures and the gradual release of local residual stresses during rapid solidification. This effect reduces the pinning effect on magnetic domain wall movement and effectively decreases the Hc of the alloy.

Just Accepted

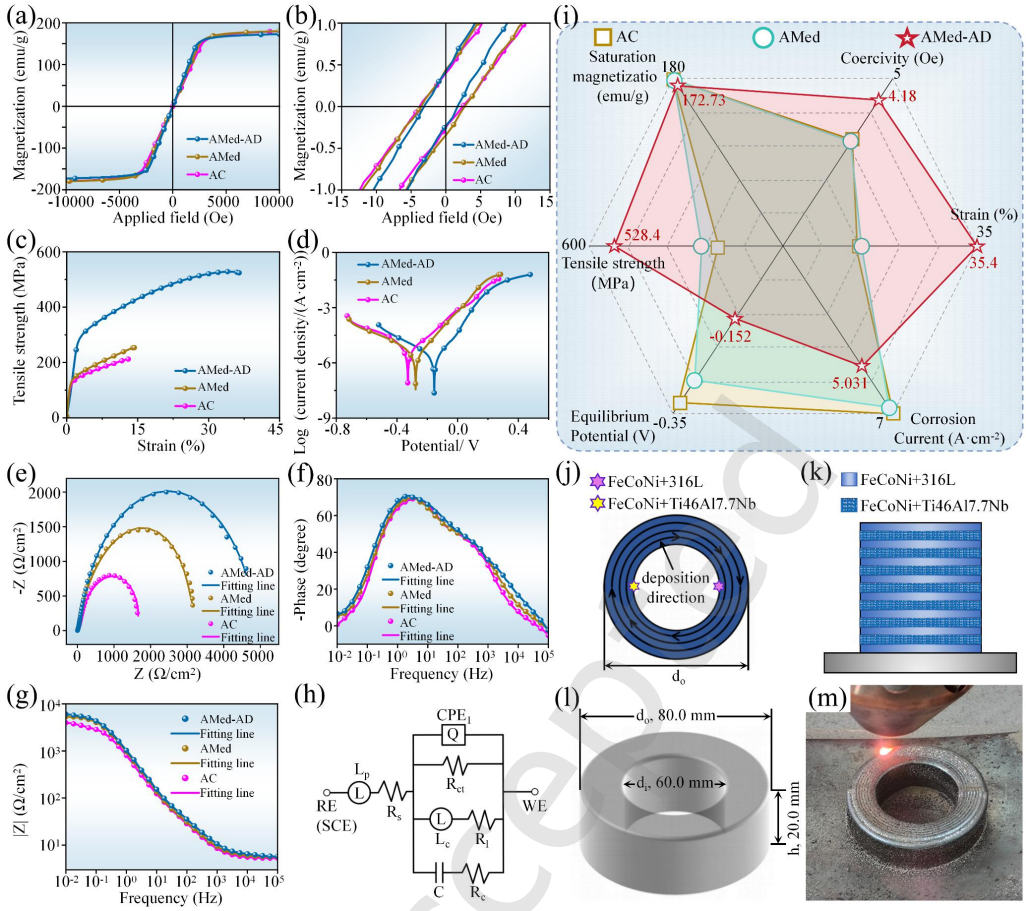


Figure 4 Comparison of the properties of three kinds of FeCoNi-based alloys: (a) Hysteresis loop at room temperature; (b) Enlargement of hysteresis near the origin; (c) Tensile engineering stress-strain curves at room temperature; (d) Dynamic potential polarization curves; EIS of the three kinds of materials in 3.5 wt% NaCl solution: (e) Nyquist plot; (f, g) Bode plot; (h) Equivalent circuit mode; (i) Comprehensive performance comparison; Deposition process schematic diagram: (j) Alternate as the starting point for depositioning; (k) Alternating combination of two kinds of alloys; (l) Final depositioned ring diagram; (m) Depositioning process.

For the DED-fabricated FeCoNi-$(316L)_{5wt.\%}$ and $(FeCoNi)Ti_2Al_2Nb_{0.33}$ alloys, the Ms values are 175.14 emu/g and 158.84 emu/g, and the corresponding Hc values are 4.91 Oe and 5.33 Oe, respectively **(Figs. S6**(a-b)). Compared with the AMed alloy,

Just Accepted

the alloys modified with 316L SS, Ti, Al, and Nb elements exhibit a significant reduction in Ms and a distinct increase in Hc. This indicates that the introduction of alloying elements leads to the deterioration of the soft magnetic properties of FeCoNi-based alloys, which is mainly because the Ms is predominantly determined by the chemical composition of the alloy [44]. Specifically, a high concentration of ferromagnetic elements (Fe, Co, and Ni) contributes to a large total atomic magnetic moment per unit mass, thereby yielding a high Ms. With the incorporation of non-ferromagnetic elements (Cr and Mo in 316L SS, as well as doped Ti, Al, and Nb), these solute atoms dissolve into the matrix lattice and occupy the lattice sites originally belonging to ferromagnetic atoms. Owing to the unique outer electron configuration of non-ferromagnetic elements, they provide negligible or even negative contributions to the total magnetic moment, which reduces the average magnetic moment of the alloy system and manifests as a macroscopic decline in Ms. This phenomenon is defined as the magnetic dilution effect [45-47]. The Hc of soft magnetic materials is highly sensitive to microstructural features, and its variation is predominantly determined by the motion behavior of magnetic domain walls. A close correlation exists between Hc and grain size. For conventional soft magnetic materials, when the grain size exceeds the thickness of magnetic domain walls, the Hc generally follows the relationship of $Hc \propto 1/Dg$ with grain size (Dg) [48]. In this case, grain boundaries act as effective pinning sites for magnetic domain wall migration. Grain refinement increases the total grain boundary area and enhances the pinning effect on domain walls, which ultimately leads to an increase in Hc.

The alloy system reinforced with 316L SS exhibits overall superior soft magnetic properties compared to the alloy modified with Ti, Al, and Nb elements. This discrepancy can be elaborated from two perspectives. On the one hand, in terms of

Just Accepted

compositional characteristics, 316L SS contains high proportions of Fe and Ni elements. When incorporated into the FeCoNi alloy, it introduces non-ferromagnetic Cr and a small amount of Mo while supplementing Fe and Ni simultaneously, resulting in a relatively mild reduction in the total concentration of ferromagnetic elements within the alloy. In contrast, Ti, Al, and Nb are typical non-ferromagnetic elements. Their direct addition substantially dilutes the content of Fe, Co, and Ni in the matrix, thereby inducing a more prominent magnetic dilution effect. On the other hand, from the perspective of microstructural characteristics, distinct honeycomb-like cellular structures are formed in the alloy system doped with Ti, Al, and Nb elements, and such cellular structures become more prominent with the increase in alloying element content. These unique cellular microstructures can hinder the migration of magnetic domain walls, thereby leading to a remarkable increase in Hc. In comparison, although the 316L-modified alloy also undergoes grain refinement, its microstructural evolution is relatively moderate without the formation of complex cellular structures, which results in a weaker pinning effect on magnetic domain walls.

The Ms and Hc of the AMed-AD alloy are intermediate between those of the FeCoNi-$(316L)_{5wt.\%}$ alloy and the $(FeCoNi)Ti_2Al_2Nb_{0.33}$ alloy, presenting an intermediate state of magnetic performance. The alloy exhibits a Ms of approximately 172.73 emu/g and a Hc of 4.18 Oe. This performance characteristic originates from the simultaneous introduction of the two aforementioned types of components in the alternately composite structure. The coexistence of 316L component with a weak magnetic dilution effect and Ti/Al/Nb component with a strong magnetic dilution effect enables the effective concentration of ferromagnetic elements and the corresponding magnetic moment contribution of the AMed-AD alloy to fall between

Just Accepted

those of the two single-modified alloys, thereby achieving an intermediate level of Ms. As a microstructure-sensitive magnetic parameter, Hc is predominantly governed by the pinning effect of internal defects, precipitated phases, grain boundaries, and other microstructural features on the migration of magnetic domain walls. The FeCoNi-$(316L)_{5wt.\%}$ alloy exhibits a mild microstructural evolution, which only undergoes simple grain refinement without complex microstructural changes. In contrast, numerous densely dispersed nano-sized $(Fe,Co,Ni)_3Al$ precipitates are formed in the $(FeCoNi)Ti_2Al_2Nb_{0.33}$ alloy. These precipitates construct coherent interfaces with the alloy matrix and exert a strong pinning effect on magnetic domain walls. Furthermore, the formation of honeycomb-like cellular structures in this alloy also impedes the migration of magnetic domain walls, and the above microstructural evolutions collectively contribute to the increased Hc. The AMed-AD alloy possesses a microstructure featuring the characteristics of the two single-modified alloys, resulting in a moderate pinning strength on magnetic domain walls between the two counterparts. Consequently, its Hc presents an intermediate level among the three alloy systems.

3.4 Mechanical properties

The tensile stress-strain curves of FeCoNi-based soft magnetic alloys are displayed in Fig. 4(c). It can be observed that the AC alloy possesses an ultimate tensile strength of approximately 211.3 MPa and an elongation of about 12.7%. Comparative analysis demonstrates that the AMed alloy exhibits an ultimate tensile strength of 253.7 MPa and an elongation of 14.3%. The results indicate that the DED process significantly optimizes the mechanical properties of FeCoNi soft magnetic alloys. The alloy fabricated by the DED process achieves a substantial improvement

Just Accepted

in ultimate tensile strength, along with a pronounced enhancement in plastic deformation capacity (elongation), realizing the synchronous improvement of strength and plasticity and demonstrating excellent comprehensive mechanical properties. The extremely high cooling rate of the DED process effectively restricts grain growth and induces prominent grain refinement. The refined grain structure improves the material strength by increasing the grain boundary density and hindering dislocation slip. Meanwhile, it promotes coordinated intergranular deformation during plastic deformation, which effectively delays the initiation and propagation of microcracks. Meanwhile, the rapid solidification process effectively eliminates common casting defects in traditional manufacturing, including macroscopic elemental segregation, shrinkage cavities, and porosity, thereby achieving uniform compositional distribution and dense microstructure of the alloy. This optimization reduces stress concentration sites and crack initiation sources, enabling the alloy to withstand greater plastic deformation during tensile loading and avoid premature fracture. In addition, the cyclic thermal cycling during layer-by-layer deposition serves as multiple in-situ heat treatments for the pre-deposited layers. This effect facilitates the partial release of residual stress, optimizes the internal stress state of the material, and prevents premature brittle fracture caused by excessive residual tensile stress.

As observed in Fig. S6(c), the alloyed materials exhibit a significant improvement in ultimate tensile strength but a declining trend in elongation compared with the pristine alloy. This variation is mainly attributed to the solid solution strengthening effect induced by the introduction of alloying elements. The incorporation of solute atoms triggers severe lattice distortion in the crystal structure, which effectively hinders dislocation movement and thereby enhances the tensile strength of the alloy. Nevertheless, such a strengthening mechanism is usually

Just Accepted

achieved at the expense of plastic deformation capacity, leading to a reduction in elongation. Furthermore, excessive addition of alloying elements may induce the precipitation of secondary phases and grain boundary embrittlement, which further exacerbates the deterioration of the alloy plasticity.

Compared with the FeCoNi-$(316L)_{5wt.\%}$ alloy, the alloy doped with Ti, Al, and Nb elements delivers a higher ultimate tensile strength but a remarkably reduced elongation. The discrepancy in strength and plasticity is primarily governed by the distinct strengthening mechanisms of different alloying elements and their varied effects on microstructural evolution. As potent intermetallic-forming elements, Ti, Al, and Nb tend to induce the precipitation of fine and densely dispersed secondary phase particles within the alloy matrix. These precipitates can effectively pin dislocations and generate a pronounced precipitation strengthening effect, which substantially improves the ultimate tensile strength of the material. However, this strengthening mechanism is generally achieved at the expense of ductility. The hard secondary phase particles act as stress concentration sites, facilitating the initiation and coalescence of microvoids within the matrix. Meanwhile, these particles hinder the uniform slip of dislocations, degrade the uniform deformation capacity of the material, and consequently result in a reduced elongation. In contrast, the incorporation of 316L SS mainly introduces alloying elements including Fe, Ni, Cr, and Mo. These elements improve the alloy strength primarily by stabilizing the austenitic matrix, and their detrimental effect on plasticity is considerably weaker than that of precipitation strengthening induced by hard secondary phases.

As observed in Fig. 4(c), the AMed-AD alloy possesses an ultimate tensile strength of approximately 528.4 MPa, a yield strength of 269.3 MPa, and an elongation of 35.4%. Compared with the AC alloy, its ultimate tensile strength, yield

Just Accepted

strength, and elongation are increased by approximately 150%, 120%, and 179%, respectively, achieving a simultaneous enhancement of strength and plasticity. It can be concluded that the FeCoNi-based alloy fabricated by alternately deposition of two composite powders inherits the high-strength characteristics of the $(FeCoNi)Ti_2Al_2Nb_{0.33}$ alloy and retains the excellent ductility of the $FeCoNi\text{-}(316L)_{5wt.\%}$ alloy. Consequently, a superior strength-plasticity synergy is realized in the developed alternating composite alloy. The realization of this synergistic effect is mainly attributed to the formation of a heterogeneous layered structure with alternating hard and soft domains within the material. Specifically, the $(FeCoNi)Ti_2Al_2Nb_{0.33}$ layer acts as the hard layer to bear major applied loads, which achieves prominent precipitation strengthening via the formation of high-density nano-sized strengthening precipitates. In contrast, the $FeCoNi\text{-}(316L)_{5wt.\%}$ layer possesses a low stacking fault energy and readily induces mechanical twins during deformation, serving as the soft layer that endows the composite alloy with excellent plastic deformability. During tensile deformation, the significant yield strength mismatch between adjacent hard and soft layers promotes the accumulation of a large number of geometrically necessary dislocations at the heterogeneous interfaces. This unique interfacial strengthening behavior substantially improves the overall work-hardening rate and effectively suppresses local plastic instability, thereby enabling the outstanding strength-ductility synergy of the AMed-AD alloy. Meanwhile, the layered heterogeneous interfaces can effectively blunt and deflect the crack propagation path. When cracks initiate in the hard layers and propagate toward the soft layers, the soft layers undergo sufficient plastic deformation to blunt the crack tips and further consume fracture energy. Through the rational design of heterogeneous interfaces and the coordinated deformation of multiple strengthening

Just Accepted

mechanisms, the AMed-AD alloy achieves an excellent balance between strength and ductility, offering an effective microstructural regulation strategy for performance optimization and synergistic property enhancement of advanced soft magnetic alloys.

To further clarify the root causes of the differences in tensile properties and the failure mechanisms, the fracture surfaces of the AC and AMed-AD specimens were examined using SEM and 3D Measuring Microscope. The fracture surface of the AC alloy exhibits a classic "rock candy" morphology, composed of numerous smooth, grain boundary facets (**Figs. 5**(a_1–a_2)). At higher magnification, these facets appear relatively smooth and flat, revealing that the crack propagated along the grain boundaries rather than through the grain interiors (Fig. 5(a_3)). This indicates that the primary failure mode of the AC alloy was intergranular fracture. Conversely, the AMed-AD alloy fracture surface is marked by abundant voids and dimples (Figs. 5(b_1–b_2)), signifying a typical dimple fracture surface and ductile fracture mode. The presence of extensive equiaxed dimples, formed by microvoid coalescence under normal stress, alongside localized shear dimples at the edges (Fig. 5(b_3)), correlates well with the alloy superior tensile ductility. Further analyses were conducted based on **Fig. S7**, with detailed descriptions provided in the **Supplementary Materials**.

The tensile mechanism is depicted in Figs. 5(c–d). AC alloy exhibits a coarse equiaxed grain structure, demonstrating extremely limited plastic deformation capacity in the tensile direction. The grains remain equiaxed after tension, and the fracture mode is mainly characterized by intergranular fracture (Figs. 5(c_1–c_2)). In contrast, the AMed-AD alloy undergoes significant plastic deformation along the tensile direction, with the grain morphology being noticeably elongated. Its strengthening mechanism is primarily attributed to the hindrance of dislocation slip by the cellular structure and the pinning effect on dislocation motion by the dispersed

Just Accepted

nano-scale precipitates. The synergistic effect of these two factors effectively inhibits the propagation of stress within the alloy, thereby significantly enhancing the strength (Figs. 5(d_1–d_2)).

3.5 Corrosion resistance properties

The corrosion resistance of FeCoNi-based soft magnetic alloys was tested at room temperature, and the corresponding potentiodynamic polarization curves are displayed in Fig. 4(d). All polarization curves exhibit typical activation-passivation characteristics. The AC alloy presents the most negative self-corrosion potential of approximately -0.331 V and a corrosion current density of 4.158×10^{-6} A·cm^{-2}, with no obvious passivation platform observed in the anodic polarization region. In comparison, the AMed alloy possesses a self-corrosion potential of approximately -0.275 V and a corrosion current density of 5.031×10^{-6} A·cm^{-2}.

The self-corrosion potential characterizes the thermodynamic tendency of material corrosion, where a more positive potential corresponds to a stronger corrosion resistance. The corrosion current density reflects the kinetic corrosion behavior, and a lower value indicates a slower corrosion rate [49, 50]. Combined with the above electrochemical parameters, the AMed alloy exhibits superior corrosion resistance compared with the AC alloy.

This advantage is attributed mainly to two factors. First, the ultra-high cooling rate of DED suppresses elemental diffusion during solidification and homogenizes the composition, which not only mitigates micro-galvanic corrosion caused by compositional inhomogeneity but also provides a structural prerequisite for forming a continuous, stable passive film. Second, rapid solidification refines the grains and increases grain-boundary density, thereby promoting uniform distribution of

Just Accepted

passivating elements and accelerating passive-film formation. Consequently, the passive film on the DED alloy is more intact and protective than the discontinuous, porous, defective layers typically formed on the as-cast surface, which markedly enhances resistance to both uniform and localized corrosion.

As observed from Fig. S6(d), the (FeCoNi)$Ti_2Al_2Nb_{0.33}$ alloy exhibits a self-corrosion potential of approximately -0.191 V and a corrosion current density of 6.516×10^{-6} A·cm^{-2}. This indicates that the incorporation of Ti, Al, and Nb elements promotes the formation of passive films and improves the corrosion resistance of the alloy to a certain extent. For the FeCoNi-$(316L)_{5wt.\%}$ alloy, the self-corrosion potential and corrosion current density are measured to be approximately -0.139 V and 7.024×10^{-6} A·cm^{-2}, respectively. Based on the above comprehensive analysis, the FeCoNi-$(316L)_{5wt.\%}$ alloy delivers the optimal corrosion resistance among all tested alloy systems.

The AC and AMed alloy lacks efficient passivating elements, making it difficult to form a dense and stable passive film on the material surface; both alloys therefore undergo primarily active dissolution and exhibit inferior corrosion resistance. The (FeCoNi)$Ti_2Al_2Nb_{0.33}$ alloy contains Ti, Al and Nb with moderate passivating ability, but these elements tend to precipitate as intermetallic compounds in the matrix, yielding a discontinuous and structurally unstable passive film. Its corrosion resistance is thus improved over the AC alloy but remains limited. In contrast, the FeCoNi-$(316L)_{5wt.\%}$ alloy introduces efficient passivating elements such as Cr and Mo, which are well compatible with the FeCoNi matrix and favor a continuous, dense, highly stable passive film. This optimized layer effectively suppresses the initiation of localized corrosion, endowing the alloy with the best corrosion resistance.

The AMed-AD alloy exhibits a self-corrosion potential of approximately -0.152

Just Accepted

V and a corrosion current density of 6.731×10^{-6} A·cm^{-2}. The electrochemical test results demonstrate that its corrosion resistance is intermediate between that of the (FeCoNi)$Ti_2Al_2Nb_{0.33}$ alloy and the FeCoNi-$(316L)_{5wt.\%}$ alloy. The underlying reasons for this intermediate corrosion performance are elaborated as follows. Firstly, the composite alloy simultaneously incorporates high-efficiency passivating elements (Cr and Mo) derived from 316L SS and minor passivating elements including Ti, Al, and Nb. The presence of Cr and Mo provides a crucial foundation for the formation of continuous and dense passive films, endowing the composite alloy with remarkably better corrosion resistance than the (FeCoNi)$Ti_2Al_2Nb_{0.33}$ alloy that relies merely on Ti, Al, and Nb for passivation. However, the relatively low content of Cr and Mo in the composite alloy restricts the compactness and structural stability of the passive film, which fails to reach the superior passivation level of the FeCoNi-$(316L)_{5wt.\%}$ alloy with sufficient high-efficiency passivating elements. Secondly, the alternately deposition process integrates the dual advantages of rapid solidification and heterogeneous structure construction. The rapid solidification effect significantly refines the grain microstructure, increases the grain boundary density, and homogenizes the elemental distribution within the alloy. Moreover, the constructed heterogeneous multilayer structure facilitates the rapid nucleation and spreading of passive films during the corrosion process. Meanwhile, the heterogeneous interfaces regulate the local electrochemical environment and inhibit the initiation and propagation of pitting corrosion, thereby effectively improving the continuity and stability of the overall passive film.

To corroborate the corrosion resistance, electrochemical impedance spectroscopy (EIS) was performed [51]. Fig. 4(e) shows the Nyquist plot, with the real part Z' on the horizontal axis and the imaginary part Z'' on the vertical axis; a larger

Just Accepted

capacitive-loop radius indicates higher corrosion resistance [52], in agreement with the potentiodynamic polarization results [53]. Figures 4(f-g) present the fitted Bode plots for the three alloys. In the low-frequency region (10^{-2} to 10^{0} Hz), |Z| reaches its maximum, indicating a dense passive film at the interface. In the mid-frequency region (10^{0} to 10^{2} Hz), the |Z| slope approaches −1 and the phase angle peaks. In the high-frequency region (10^{2} to 10^{5} Hz), the |Z| slope tends toward zero and the phase angle approaches 0°, reflecting that solution resistance dominates the impedance response. A higher |Z| and a larger phase angle both indicate stronger resistance to electrolyte penetration and thus better corrosion resistance [54]. Comparison of |Z| and the phase angle confirms that the AMed-AD alloy exhibits the best corrosion resistance, consistent with the potentiodynamic polarization and Nyquist results.

The equivalent circuit for data fitting is shown in Fig. 4(h) [55]. Here, R_s represents the solution resistance; R_{ct} and CPE_1 denote the charge transfer resistance and constant phase element; R_c and C are the polarization resistance and surface capacitance; while L_p, L_c, and R_l account for inductive components and associated loss. The detailed properties of the three FeCoNi-based soft-magnetic alloys are summarized in **Table 1**. Comparative analysis shows that the AMed-AD FeCoNi-based alloy delivers well-balanced and superior overall properties (Fig. 4(i)). The DED process for fabricating annular samples is illustrated (Figs. 4(j–k)). A high-quality, macroscopically crack-free ring was produced using an alternating start-point strategy with a uniform clockwise deposition path (Fig. 4(l)). The resulting two-layer alternating structure (Fig. 4(m)) is suitable for manufacturing critical components such as motor iron cores and generator stators.

Table 1 Magnetic, Mechanical and Corrosion resistance properties of three types of FeCoNi-based soft-magnetic alloys.

Just Accepted

Sample	AC	AMed	AMed-AD
Ms (emu/g)	179.52	179.89	172.73
Hc (Oe)	3.17	3.14	4.18
Tensile strength (MPa)	211.3	253.7	528.4
Strain (%)	12.7	14.3	35.4
Equilibrium potential (V)	-0.331	-0.275 V	-0.152
Corrosion Current ($A \cdot cm^{-2}$)	4.158×10^{-6}	5.031×10^{-6}	6.731×10^{-6}

A schematic diagram of the corrosion mechanism is presented in Figs. 5(e-f). Chloride ions adsorb onto the metal surface and consequently penetrate the passive film. It can be observed that the AC alloy exhibits relatively large corrosion pits on its surface (Figs. 5(e_1–e_2)), whereas the corrosion pits on the AMed-AD alloy are significantly smaller in size (Figs. 5(f_1–f_2)). This phenomenon is primarily attributed to two factors. On the one hand, the homogeneous microstructure effectively suppresses local galvanic corrosion induced by compositional segregation. On the other hand, the nanophases uniformly distributed within the grains act as sacrificial anodes, dissolving preferentially and thereby protecting the matrix. The synergistic effect of the two enhances the corrosion resistance of the alloy.

3.6 Insight into properties via DFT calculations

Density functional theory (DFT) calculations were performed to investigate how alloying affects the mechanical, magnetic, and electrochemical corrosion properties of FeCoNi-based alloys. Models of Ti/Nb-doped and Cr/Mo-doped FeCoNi are shown in Figs. 5(g–h), with their corresponding ELF results presented in Figs. 5(i–j). The optimized structures of γ-FeCoNi and $(Fe, Co, Ni)_3Al$ are shown in **Figs. S8**(a-b). ELF analysis (Figs. S8(c–d)) reveals that upon Ti/Nb or Cr/Mo doping, the ELF between matrix atoms increases from ~0.5 to approximately 0.7~0.9. Since ELF values of 0.5 and 1 correspond to electron-gas-like and fully localized states,

Just Accepted

respectively [56, 57], this rise signifies a shift in bond character from metallic towards covalent. The enhanced covalent interaction strengthens atomic bonding, thereby improving the mechanical properties of the FeCoNi matrix.

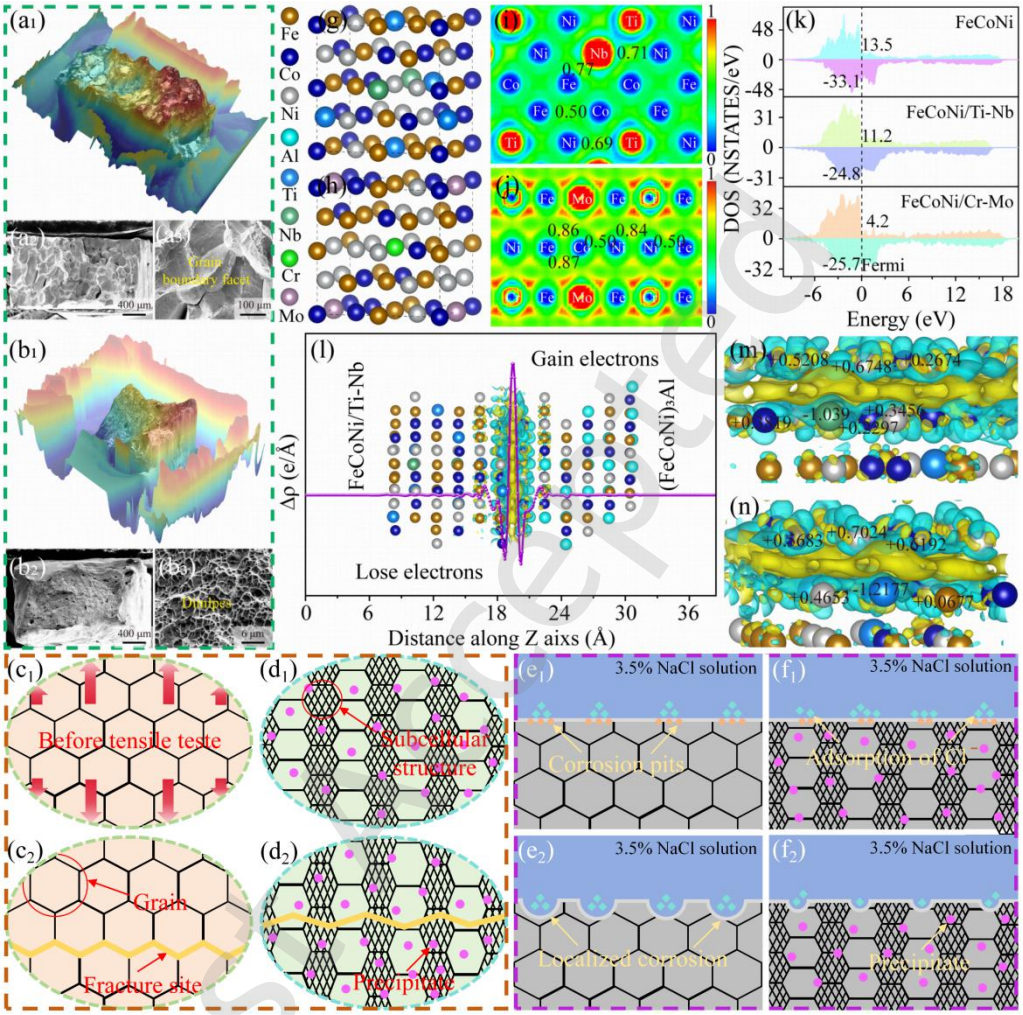


Figure 5 Fracture morphologies of the alloys and their corresponding higher-magnification images: (a_1–a_3) AC alloy; (b_1–b_3) AMed-AD alloy; (c–d/e–f) Schematic diagram of the tensile/electrochemical corrosion mechanism; DFT calculations: (g–h) Structural models of Ti/Nb-doped and Cr/Mo-doped γ-FeCoNi; Two-dimensional ELFs for the (i–j) Ti/Nb-doped and Cr/Mo-doped γ-FeCoNi; (k) Calculated total DOS of Ti/Nb-doped, Cr/Mo-doped γ-FeCoNi and γ-FeNi models; (l) Difference in the charge density of the (Fe, Co, $Ni)_3Al$(0001)//Ti/Nb-doped γ-FeCoNi(111) interfaces; (m–n) Local magnification image of difference in the

charge density and bader charge. Yellow and blue isosurfaces indicate captured and lost electrons, respectively.

Figure 5(k) shows the calculated density of states (DOS) before and after alloying. The DOS at the Fermi level is significantly lower in the Ti/Nb- and Cr/Mo-doped alloys compared to pure FeCoNi. A higher DOS at the Fermi level provides more available quantum states for electron transitions, increasing electron scattering probability and thus reducing resistivity. For soft magnetic materials, low resistivity increases eddy current losses. A low DOS at the Fermi level reduces electron scattering, thereby decreasing Hc, magnetic anisotropy, and eddy current loss, while increasing permeability. Corrosion, an interfacial electron-transfer process, is also influenced by the Fermi-level DOS. A higher value provides a greater thermodynamic driving force for corrosion, making the material more electrochemically active. Conversely, a lower DOS reduces reactivity and promotes the formation of a stable, low-conductivity passivation film, thereby enhancing corrosion resistance. Thus, alloying improves both magnetic and anti-corrosion properties.

The presence of the precipitates not only pins dislocations to enhance the strength of the matrix, but also forms a strong interfacial bonding force with the matrix, thereby improving mechanical properties. The strengthening mechanism provided by the precipitates in the FeCoNi matrix is elucidated through charge density difference (CDD) analysis. The CDD was determined using the following equation [58]:

$$\rho=\rho_{tot}-\rho_{FeCoNi}-\rho_{(FeCoNi)_3Al} \quad (1)$$

Where ρ_{tot} is the charge density of the interfacial system, and ρ_{FeCoNi} and $\rho_{(FeCoNi)_3Al}$ represent the charge densities of the FeCoNi matrix and and (Fe, Co, Ni)$_3$Al precipitate phases, respectively. The charge densities of the individual phases are obtained by translating one phase away from the interface while keeping all

Just Accepted

atomic positions fixed, consistent with the interface model. Positive and negative CDD values correspond to charge accumulation and depletion, respectively, as shown in Figs. 5(l-n). The yellow and blue isosurfaces indicate captured and lost electrons, respectively. For the FeCoNi//(Fe, Co, Ni)$_3$Al interface (Fig. 5(l)), a chargegain zone formed at the interface, which indicates that the charge density increased at the interface. Figures. 5(m-n) shows the local magnification of the differential charge at the interface and the bader charge. The Ti/Nb loses electrons at the interface, while Fe/Co/Ni gains electrons. Through the mutual transfer of electrons, a strong charge interaction is ultimately formed, which significantly improves the alloy mechanical properties.

4. Conclusions

This study demonstrates that the dual-powder alternately deposition additive manufacturing strategy is an effective approach to architecting high-performance FeCoNi-based soft magnetic alloys. By combining FeCoNi pre-alloyed powder with Ti46Al7.7Nb and 316L SS powders, the prepared alloy achieves a remarkable synergy between mechanical and functional properties. The main conclusions are:

(1) The AMed-AD alloy exhibits substantially enhanced tensile strength (528.4 MPa) and elongation (35.4%), far surpassing the as-cast counterpart. This improvement is primarily due to the in-situ formation of a honeycomb-like cellular structure and coherent (Fe, Co, Ni)$_3$Al precipitates.

(2) The magnetic properties are well preserved despite significant mechanical strengthening. This is attributed to the refined and homogeneous microstructure from rapid AM solidification, which reduces defect-induced pinning sites for magnetic domain walls.

(3) Improved corrosion resistance is achieved, resulting from microstructural

Just Accepted

refinement and chemical homogeneity promoted by the DED process, which facilitates more uniform passivation.

(4) DFT calculations reveal that alloying enhances charge localization and interfacial bonding strength, while reducing the density of states at the Fermi level, thereby jointly contributing to improved mechanical, magnetic, and anti-corrosion properties.

(5) This alternately deposition DED route enables one-piece integral cores for EV and aerospace servo motors, with internal cooling channels and profiled magnetic paths, delivering high magnetic performance at the teeth and balanced strength and corrosion resistance in the yoke.

In summary, this study demonstrates that the AMed-AD alternately deposition process constructs a periodically composition-modulated alternating composite microstructure, which effectively breaks the conventional trade-off among magnetic, mechanical and corrosion resistance properties of soft magnetic alloys and offers a new route for designing advanced multifunctional soft magnetic materials. Further systematic optimization of powder chemistry and DED process parameters is still required to better balance these three properties and promote the industrial scale-up of this technology.

Just Accepted

Acknowledgements

This work was financially supported by the National Natural Science Foundation of China (Nos. 52472235; 52102291), the State Key Laboratory for Advanced Metals and Materials (Grant No. 2026-Z08), and the Natural Science Foundation of Tianjin (Grant No. 25JCQNJC00910).

References

[1] Varga, L. K. Soft magnetic nanocomposites for high-frequency and high-temperature applications. *J. Magn. Magn. Mater*. **2007**, *316*, 442-447.

[2] Sourmail, T. Near equiatomic FeCo alloys: Constitution, mechanical and magnetic properties. *Prog. Mater. Sci*. **2005**, *50*, 816–880.

[3] Chaudhary, V.; Chaudhary, R.; Banerjee, R.; Ramanujan, R. V. Accelerated and conventional development of magnetic high entropy alloys. *Mater. Today* **2021**, *49*, 231-252.

[4] Yang, X. S.; Liu, J. N.; Cui, X. F.; Jin, G.; Liu, Z.; Chen, Y. B.; Feng, X. R. Effect of remelting on microstructure and magnetic properties of Fe-Co-based alloys produced by laser additive manufacturing. *J. Phys. Chem. Solids* **2019**, *130*, 210-216.

[5] Lemke, J. N.; Simonelli, M.; Garibaldi, M.; Ashcroft, I.; Hague, R.; Vedani, M.; Wildman, R.; Tuck, C. Calorimetric study and microstructure analysis of the order-disorder phase transformation in silicon steel built by SLM. *J. Alloy. Compd*. **2017**, *722*, 293-301.

[6] Yang, X. S.; Cui, X. F.; Jin, G.; Liu, J. N.; Chen, Y. B.; Liu, Z. Soft magnetic property of $(Fe_{60}Co_{35}Ni_5)_{78}Si_6B_{12}Cu_1Mo_3$ alloys by laser additive manufacturing. *J. Magn. Magn. Mater*. **2018**, *466*, 75-80.

[7] Olekšáková, D.; Kollár, P.; Füzer, J.; Kusý, M.; Roth, S.; Polanski, K. The influence of mechanical milling on structure and soft magnetic properties of NiFe and NiFeMo alloys. *J. Magn. Magn. Mater*. **2007**, *316*, e838-e841.

[8] Kim, E. S.; Haftlang, F.; Ahn, S. Y.; Gu, G. H.; Kim, H. S. Effects of processing parameters and heat treatment on the microstructure and magnetic properties of the in-situ synthesized Fe-Ni permalloy produced using direct energy deposition. *J. Alloy. Compd*. **2022**, *907*, 164415.

[9] Baker, I. A review of the mechanical properties of B2 compounds. *Mat. Sci. Eng A* **1995**, *192/193*, 1-13.

[10] Nartu, M. S. K. K. Y.; Dasari, S.; Sharma, A.; Chaudhary, V.; Varahabhatla, S. M.; Mantri, S. A.; Ivanov, E.; Ramanujan, R.V.; Dahotre, N.B.; Banerjee, R. Reducing coercivity by chemical ordering in additively manufactured soft magnetic Fe-Co (Hiperco) alloys. *J. Alloy. Compd*. **2021**, *861*, 157998.

[11] Wang, F.; An, X. L.; Wang, Z. W.; Wu. W. Q.; Xia, W. Z.; Ni, S.; Gu, J.; Yi, J. H.; Yang, Y.; Song, M.; Zhu, Y. T. Enhanced strength and ductility of high-entropy alloy via dislocation-mediated heterogeneous martensitic transformation. *Microstructures*. **2025**, *5*, 2025088.

Just Accepted

[12] Zhang, Y.; Zhang, M.; Li, D. Y.; Zuo, T. T.; Zhou, K. X.; Gao, M. C.; Sun, B. R.; Shen, T. D. Compositional design of soft magnetic high entropy alloys by minimizing magnetostriction coefficient in $(Fe_{0.3}Co_{0.5}Ni_{0.2})_{100-x}(Al_{1/3}Si_{2/3})_x$ system. *Metals*. **2019**, *9*, 382.

[13] Zuo, T. T.; Cheng, Y. Q.; Chen, P. Y.; Gao, Z. S.; Zhang, Y.; Liaw, P. K. Structural and magnetic transitions of CoFeMnNiAl high-entropy alloys caused by composition and annealing. *Intermetallics*. **2021**, *137*, 107298.

[14] Lu, Y. P.; Gao, X. Z.; Jiang, L.; Chen, Z. N.; Wang, T. M.; Jie, J. C.; Kang, H. J.; Zhang, Y. B. et al. Directly cast bulk eutectic and near-eutectic high entropy alloys with balanced strength and ductility in a wide temperature range. *Acta Mater*. **2017**, *124*, 143-150.

[15] Mitrica, D.; Badea, I. C.; Serban, B. A.; Olaru, M. T.; Vonica, D.; Burada, M.; Piticescu, R. R.; Popov, V. V. Complex concentrated alloys for dubstitution of critical raw materials in applications for extreme conditions. *Materials*. **2021**, *14*, 1197.

[16] Subramanian, A. T. S.; Meenalochini, P.; Sathiya, S. S. B.; Prakash, G. R. A review on selection of soft magnetic materials for industrial drives. *Mater. Today. Pro*. **2021**, *45*, 1591-1596.

[17] Ron, T.; Leon, A.; Popov, V.; Strokin, E.; Eliezer, D.; Shirizly, A.; Aghion, E. Synthesis of refractory high-entropy alloy WTaMoNbV by powder bed fusion process using mixed elemental alloying powder. *Materials* **2022**, *15*, 4043.

[18] Herzog, D.; Seyda, V.; Wycisk, E.; Emmelmann, C. Additive manufacturing of metals. *Acta Mater*. **2016**, *117*, 371-392.

[19] Kürnsteiner, P.; Wilms, M. B.; Weisheit, A.; Gault, B.; Jägle, E. A.; Raabe, D. High-strength Damascus steel by additive manufacturing. *Nature*. **2020**, *582*, 515-519.

[20] Huang, J. N.; Yang, W. Q.; Gao, Z. G.; Hou, X.; Yang, X. S. Heterostructured multi-principal element alloys prepared by laser-based techniques. *Microstructures*, **2025**, *5*, 2025021.

[21] Wolff, S. J.; Lin, S.; Faierson, E. J.; Liu, W. K.; Wagner, G. J.; Cao, J. A framework to link localized cooling and properties of directed energy deposition (DED)-processed Ti-6Al-4V. *Acta Mater*. **2017**, *132*, 106-117.

[22] Tsai, M. H. Physical properties of high entropy alloys. *Entropy* **2013**, *15*, 5338-5345.

[23] Chen, T.; Chen, W. P.; Jiang, Z. F.; Zhu, D. Z.; Fu, Z. Q. An in-situ formed

Just Accepted

TiC/FeCoNi medium-entropy composite with excellent combination of mechanical and soft magnetic properties. *Vacuum* **2023**, *218*, 112601.

[24] Zou, Q.; Li, B.; Yin, J. Y.; Zhu, L. L.; Cai, G. M. Achieving mechanical-magnetic $(FeCoNi)_{86}Al_4Cu_3Ti_7$ HEAs. *Mater. Res. Bull*. **2025**, *189*, 113476.

[25] Li, P. P.; Wang, A.; Liu, C. T. Composition dependence of structure, physical and mechanical properties of $FeCoNi(MnAl)_x$ high entropy alloys. *Intermetallics* **2017**, *87*, 21-26.

[26] Sjölander, E.; Seifeddine, S. The heat treatment of Al-Si-Cu-Mg casting alloys. *J. Mater. Process. Tech*. **2010**, *210*, 1249-1259.

[27] Xue, H.; Liang, Y. F.; Peng, H.; Wang, Y. L.; Lin, J. P. Additive manufacturing of micro/nano multiphase synergistically reinforced Ti-55Al-7.5Nb with a reticular boundary precipitate via direct laser deposition. *Addit. Manuf*. **2022**, *58*, 102989.

[28] Zhao, J. F.; Wang, H. P. Twin interface structures and formation mechanisms of the topologically close-packed phase within refractory Nb-Ni binary alloy. *T. Mater. Res.* **2025**, *1*, 100070.

[29] Sun, S. S.; Teng, Q.; Xie, Y.; Liu, T.; Ma, R.; Bai, J.; Cai, C.; Wei, Q. S. Two-step heat treatment for laser powder bed fusion of a nickel-based superalloy with simultaneously enhanced tensile strength and ductility. *Addit. Manuf*. **2021**, *46*, 102168.

[30] Bobel, A.; Hector Jr, L. G.; Chelladurai, I.; Sachdev, A. K.; Brown, T.; Poling, W. A. et al. *In situ* synchrotron X-ray imaging of 4140 steel laser powder bed fusion. *Materialia* **2019**, *6*, 100306.

[31] Kresse, G.; Furthmüller, J. Efficiency of ab-initio total energy calculations for metals and semiconductors using a plane-wave basis set. *Comp. Mater. Sci*. **1996**, *6*, 15-50.

[32] Kresse, G.; Furthmüller, J. Efficient iterative schemes for ab initio total-energy calculations using a plane-wave basis set. *Phys. Rev. B* **1996**, *54*, 11169-11186.

[33] Perdew, J. P.; Burke, K.; Ernzerhof, M. Generalized gradient approximation made simple. *Phys. Rev. Lett*. **1996**, *77*, 3865-3868.

[34] Kresse, G.; Joubert, D. From ultrasoft pseudopotentials to the projector augmented-wave method. *Phys. Rev. B* **1999**, *59*, 1758-1775.

[35] Li, Z.; Xu, H.; Gu, Y.; Pan, M. X.; Yu, L. Y.; Tan, X. H.; Hou, X. L. Correlation between the magnetic properties and phase constitution of FeCoNi $(CuAl)_{0.8}$ Gax ($0 \leq x \leq 0.08$) high-entropy alloys. *J. Alloy. Compd*. **2018**, *746*, 285-291.

Just Accepted

[36] Bermingham, M. J.; StJohn, D. H.; Krynen, J.; Tedman-Jones, S.; Dargusch, M. S. Promoting the columnar to equiaxed transition and grain refinement of titanium alloys during additive manufacturing. *Acta Mater*. **2019**, *168*, 261-274.

[37] Polonsky, A. T.; Lenthe, W. C.; Echlin, M. P.; Livescu, V.; Gray III, G. T.; Pollock, T. M. Solidification-driven orientation gradients in additively manufactured stainless steel. *Acta Mater*. **2020**, *183*, 249-260.

[38] Karimi, P.; Sadeghi, E.; Ålgårdh, J.; Keshavarzkermani, A.; Esmaeilizadeh, R.; Toyserkani, E.; Andersson, J. Columnar-to-equiaxed grain transition in powder bed fusion via mimicking casting solidification and promoting in situ recrystallization. *Addit. Manuf*. **2021**, *46*, 102086.

[39] Han, B. L.; Zhang, C. C.; Feng, K.; Li, Z. G.; Zhang, X. C.; Shen, Y. et al. Additively manufactured high strength and ductility CrCoNi medium entropy alloy with hierarchical microstructure. *Mat. Sci. Eng. A* **2021**, *820*, 141545.

[40] Wang, J. Y.; Zou, J. P.; Yang, H. L.; Zhang, L. J.; Liu, Z. L.; Dong, X. X.; Ji, S. X. Exceptional strength-ductility synergy of additively manufactured CoCrNi medium-entropy alloy achieved by lattice defects in heterogeneous microstructures. *J. Mater. Sci. Technol*. **2022**, *127*, 61-70.

[41] Wang, J. Y.; Zou, J. P.; Yang, H. L.; Liu, Z. L.; Ji, S. X. High strength and ductility of an additively manufactured CrCoNi medium-entropy alloy achieved by minor Mo doping. *Mat. Sci. Eng. A* **2022**, *843*, 143129.

[42] Yao, N.; Lu, T. W.; Feng, K.; Sun, B. H.; Wang, R. Z.; Wang, J. et al. Ultrastrong and ductile additively manufactured precipitation-hardening medium-entropy alloy at ambient and cryogenic temperatures. *Acta Mater*. **2022**, *236*, 118142.

[43] Thapliyal, S.; Agrawal, P.; Agrawal, P.; Nene, S. S.; Mishra, R. S.; McWilliams, B. A.; Cho, K. C. Segregation engineering of grain boundaries of a metastable Fe-Mn-Co-Cr-Si high entropy alloy with laser-powder bed fusion additive manufacturing. *Acta Mater*. **2021**, *219*, 117271.

[44] Garibaldi, M.; Ashcroft, I.; Hillier, N.; Harmon, S. A. C.; Hague, R. Relationship between laser energy input, microstructures and magnetic properties of selective laser melted Fe-6.9%wt Si soft magnets. *Mater. Charact*. **2018**, *143*, 144-151.

[45] Liu, Z. H.; Dong, Y. Q.; Liu, X. C.; Lu, H.; Wu, Y.; Zhang, R. H. et al. Optimizing soft magnetic properties by reducing internal defects and residual stress of $Fe_{85-x}Si_{9.6}Al_{5.4}Sn_x$ soft magnetic composites. *J. Mater. Res. Technol*. **2022**, *18*, 3872-3883.

Just Accepted

[46] Tan, X. H.; Tang, Y. J.; Tan, Y. F.; Deng, Q.; Jiao, H. S.; Yang, Y.; Xu, H. Correlation between microstructure and soft magnetic parameters of Fe-Co-Ni-Al medium-entropy alloys with FCC phase and BCC phase. *Intermetallics* **2020**, *126*, 106898.

[47] Wang, T.; Ma, Q.; Song, S. H. Highly enhanced magnetic properties of $BiFeO_3$ nanopowders by aliovalent element Ba-Zr co-doping. *J. Magn. Magn. Mater*. **2018**, *465*, 375-380.

[48] Herzer, G. Modern soft magnets: Amorphous and nanocrystalline materials. *Acta Mater*. **2013**, *61*, 718-734.

[49] Lu, Q. Q.; Chen, X. H.; Tian, W.; Wang, H.; Liu, P.; Zhou, H. L. et al. Corrosion behavior of a non-equiatomic CoCrFeNiTi high-entropy alloy: A comparison with 304 stainless steel in simulated body fluids. *J. Alloy. Compd*. **2022**, *897*, 163036.

[50] Zhang, M. D.; Shi, X. L.; Li, Z. Y.; Xu, H. Q.; Li, G. Corrosion behaviors and mechanism of $CrFeNi_2$ based high-entropy alloys. *Corros. Sci*. **2022**, *207*, 110562.

[51] Bommersbach, P.; Alemany-Dumont, C.; Millet, J. P.; Normand, B. Formation and behaviour study of an environment-friendly corrosion inhibitor by electrochemical methods. *Electrochim. Acta*. **2005**, *51*, 1076-1084.

[52] Wang, Y. J.; Hao, E. K.; Zhao, X. Q.; Xue, Y.; An, Y. L.; Zhou, H. D. Effect of microstructure evolution of Ti6Al4V alloy on its cavitation erosion and corrosion resistance in artificial seawater. *J. Mater. Sci. Technol*. **2022**, *100*, 169-181.

[53] Wu, J.; Cui, J. P.; Zheng, Q. J.; Zhang, S. D.; Sun, W. H.; Yang, B. J.; Wang, J. Q. Insight into the corrosion evolution of Fe-based amorphous coatings under wet-dry cyclic conditions. *Electrochim. Acta* **2019**, *319*, 966-980.

[54] Liu, X. Y.; Chen, S. Y.; Zhang, J. J.; Yang, G.; Zhang, Y.; Wang, T.; Lei, J. B. Enhancement of the electrochemical corrosion resistance of Ti6Al4V alloy reinforced by nano- and micro-TiC particles through directed energy deposition. *Corros. Sci*. **2023**, *221*, 111343.

[55] Yu, D. Y.; Tian, J. T.; Dai, J. H.; Wang, X. Corrosion resistance of three-layer superhydrophobic composite coating on carbon steel in seawater. *Electrochim. Acta* **2013**, *97*, 409-419.

[56] Shi, S. X.; Zhu, L. G.; Zhang, H.; Sun, Z. M.; Ahuja, R. Mapping the relationship among composition, stacking fault energy and ductility in Nb alloys: A first-principles study. *Acta Mater*. **2018**, *144*, 853-861.

[57] Xue, H.; Liang, Y. F.; Shang, S. L.; Liu, Z. K.; Lin, J. P. Atomic-scale unveiling

Just Accepted

of strengthening in interstitial solid soluted Nb-rich TiAl alloys. *J. Alloy. Compd*. **2022**, *917*, 165484.

[58] Li, Y.; Dai, J. H.; Song, Y. First-principles investigation on stability and oxygen adsorption behavior of a O/B2 interface in Ti_2AlNb alloys. *J. Alloy. Compd*. **2020**, *818*, 152926.

Just Accepted

Electronic Supplementary Material

Architecting honeycomb-like multistage structures via dual-powder alternately deposition additive manufacturing for enhanced FeCoNi soft magnetic alloys

Hui Xue [1, *], Jianda Chen [1, 2, 4, *], Shuai Hu [3,4], Ping Wang [3,4], Zhengyang Yu [1], Lei Wang [2], Delin Zhang [3,4], Yong Jiang [3,4,*]

[1] School of Mechanical Engineering, Tiangong University, Tianjin 300387, China

[2] School of Materials Science and Engineering, Tiangong University, Tianjin 300387, China

[3] School of Electronic and Information Engineering, Tiangong University, Tianjin 300387, China

[4] Institute of Quantum Materials and Devices, Tiangong University, Tianjin 300387, China

✉Address correspondence to Hui Xue, xuehui@tiangong.edu.cn; Jianda Chen, 18622511438@163.com; Yong Jiang, yjiang@tiangong.edu.cn

Supporting information to https://doi.org/10.26599/NR.2026.94909250

Just Accepted

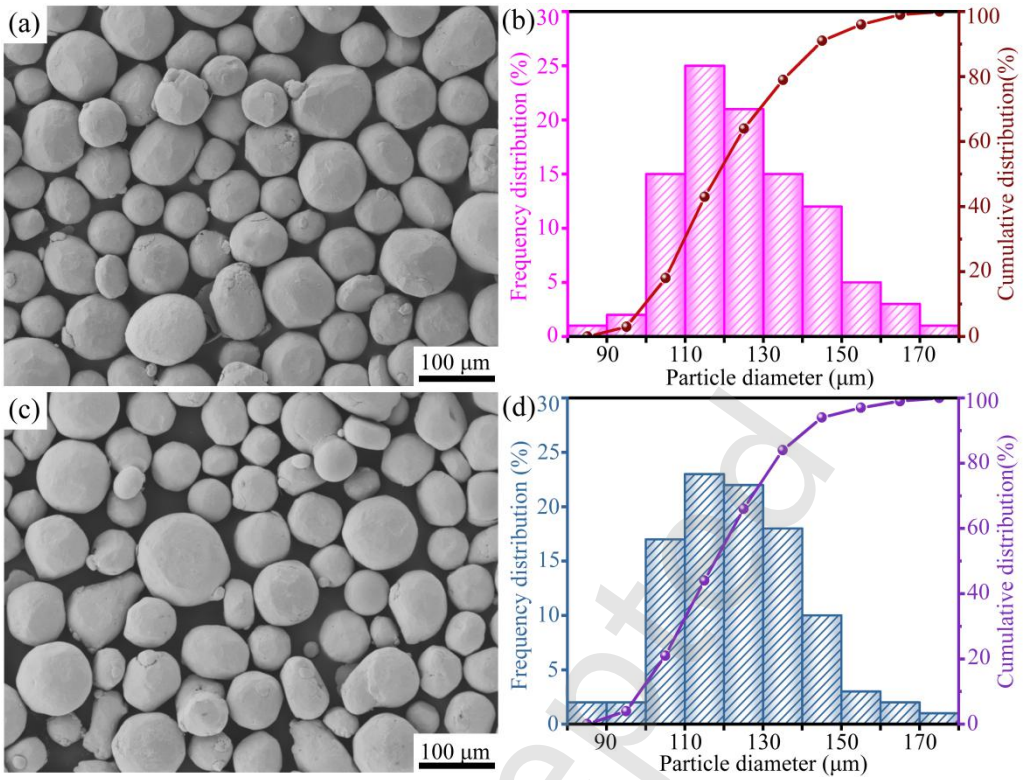


Figure S1 (a-b) The morphology and grain size statistics of Ti-46Al-7.7Nb pre-alloy powders; (c-d) The morphology of 316L SS pre-alloy powders.

Compared with the AC alloy, the alloy modified with 5 wt.% 316L SS exhibits more distinct melt pool boundaries accompanied by slightly reduced melt pool dimensions, and a denser fish-scale stacked structure is formed. Its microstructure features a coexistence of columnar grains and a small quantity of equiaxed grains. Although the grain orientation remains predominantly perpendicular to the melt pool boundaries, the overall densification of the alloy is improved (**Figs. S2**(a_1-a_2)). This indicates that the incorporation of 316L SS elevates the alloying degree of the matrix and increases the nucleation rate during solidification, thereby restraining grain coarsening to a certain extent. Meanwhile, grain boundaries become clearer with irregular morphologies, and microstructural homogeneity is enhanced. Only a small

Just Accepted

number of pores can be detected in localized regions, and no obvious precipitation of secondary phases is observed. In comparison, the (FeCoNi)$Ti_2Al_2Nb_{0.33}$ alloy exhibits a remarkable grain refinement effect: the melt pool size is further reduced with highly tortuous and intricate melt pool boundaries, and the interlayer overlapping effect is intensified, giving rise to a distinct honeycomb cellular structure (Figs. S2(b_1-b_2)). A large number of fine and uniform columnar grains are observed in the microstructure, which are predominantly oriented perpendicular to the melt pool boundaries. The overall microstructural homogeneity and densification degree are substantially superior to those of the former two alloys. This phenomenon can be attributed to the incorporation of Ti, Al and Nb elements. During solidification, these elements promote the formation of fine secondary phase particles, which effectively hinder grain growth and thereby achieve efficient microstructural refinement.

Just Accepted

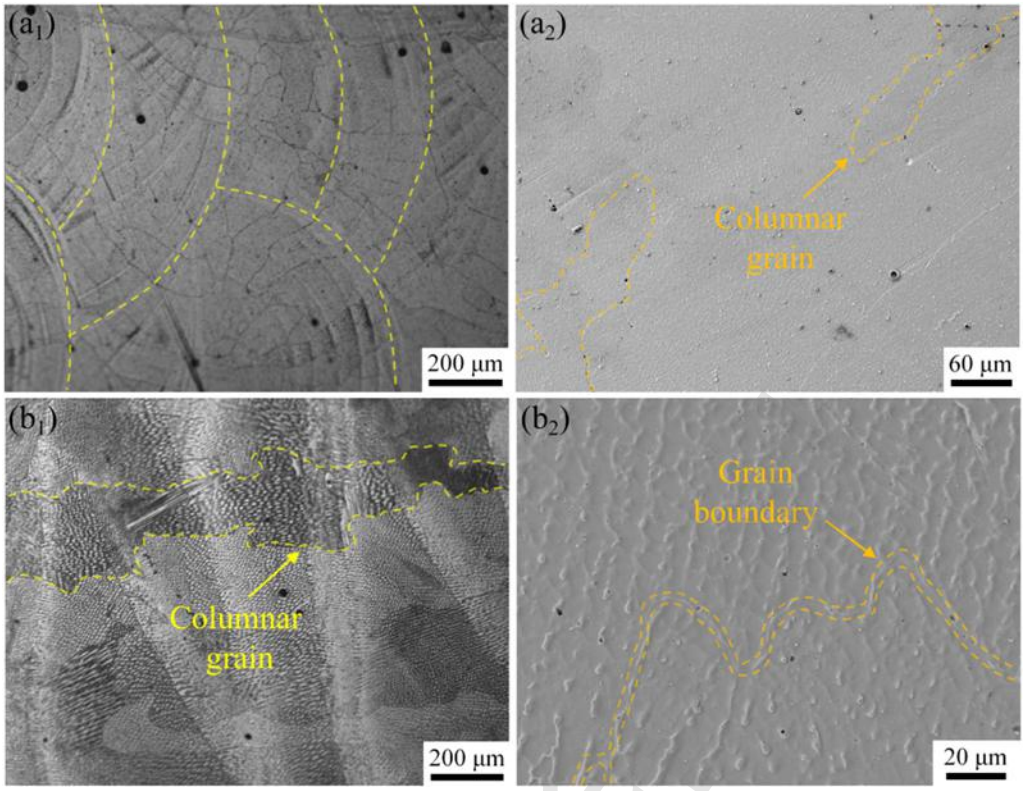


Figure S2 Microstructures for the FeCoNi-(316L)$_{5wt.\%}$/FeCoNi-(Ti46Al7.7Nb)$_{2at.\%}$ alloy: (a) metallographic microstructure; (b) SEM images

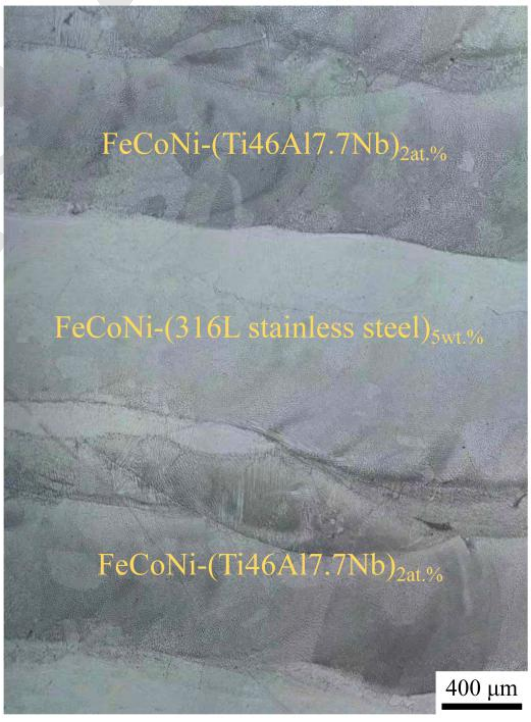


Figure S3 Metallographic microstructure for the AMed-AD FeCoNi-based alloy.

Just Accepted

For the FeCoNi-$(316L)_{5wt.\%}$ alloy, the grain orientation distribution is more homogeneous, with the fractions of red, green, and blue grains reaching a balanced state and further enhanced orientation randomness, while no obvious increment in texture intensity is detected (**Fig. S4**(a_1)). Although its grain size is reduced compared with that of the AMed alloy, the orientation distribution remains dominated by random characteristics. This result demonstrates that the incorporation of 316L can effectively increase the nucleation rate and refine grains, whereas it fails to induce substantial preferential grain growth. Instead, it facilitates the formation of columnar microstructures with more uniform grain orientations.

By contrast, the alloy modified with Ti, Al, and Nb elements exhibits a weak (001) preferential orientation. The dominant red regions in the IPF maps indicate that the (001) crystallographic direction of the grains is parallel to the building direction, resulting in the formation of a directional solidification texture (Fig. S4(b_1)). Meanwhile, the unique honeycomb-like cellular structure of this alloy is manifested as a dense stacking of numerous fine red grains in the IPF images, which substantially improves the microstructural homogeneity. Notably, although the alloy is predominated by the (001) orientation, sporadic green and blue grains can still be observed in localized regions. This indicates that certain orientation diversity is retained even under the condition of strong preferential orientation, providing a viable structural basis for the performance regulation of the alloy.

Just Accepted

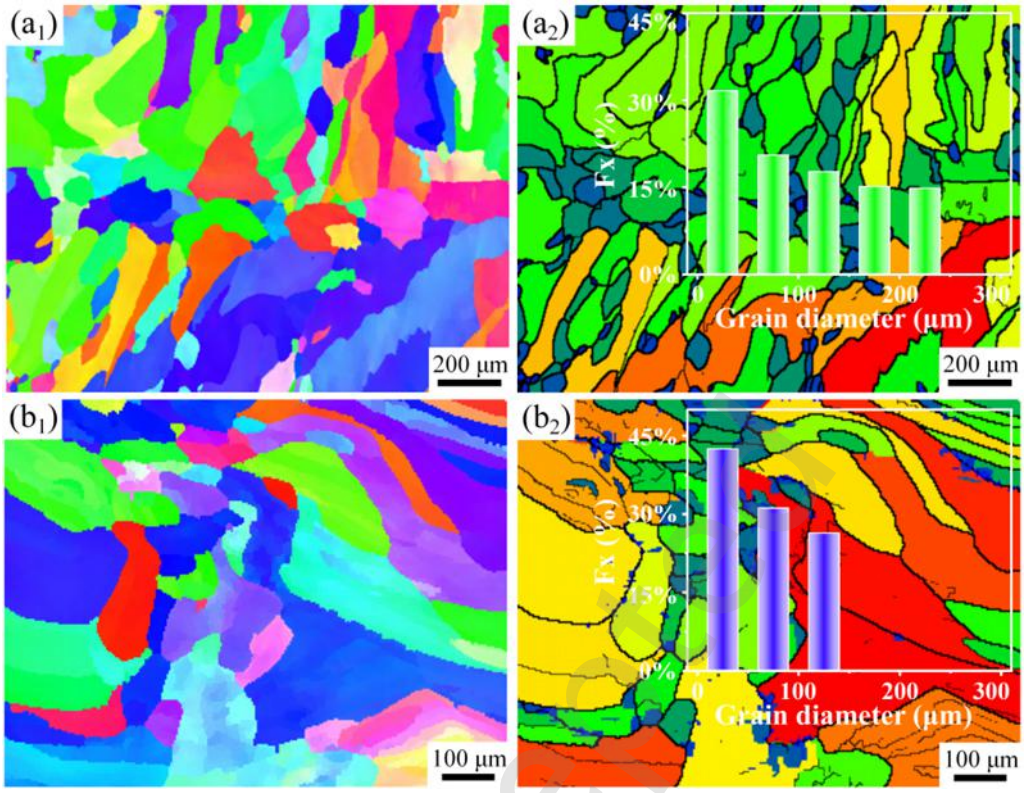


Figure S4 Microstructures for the FeCoNi-$(316L)_{5\ wt.\%}$/FeCoNi-$(Ti46Al7.7Nb)_{2\ at.\%}$ alloy: (a) IPF images; (b) grain size distribution images.

Just Accepted

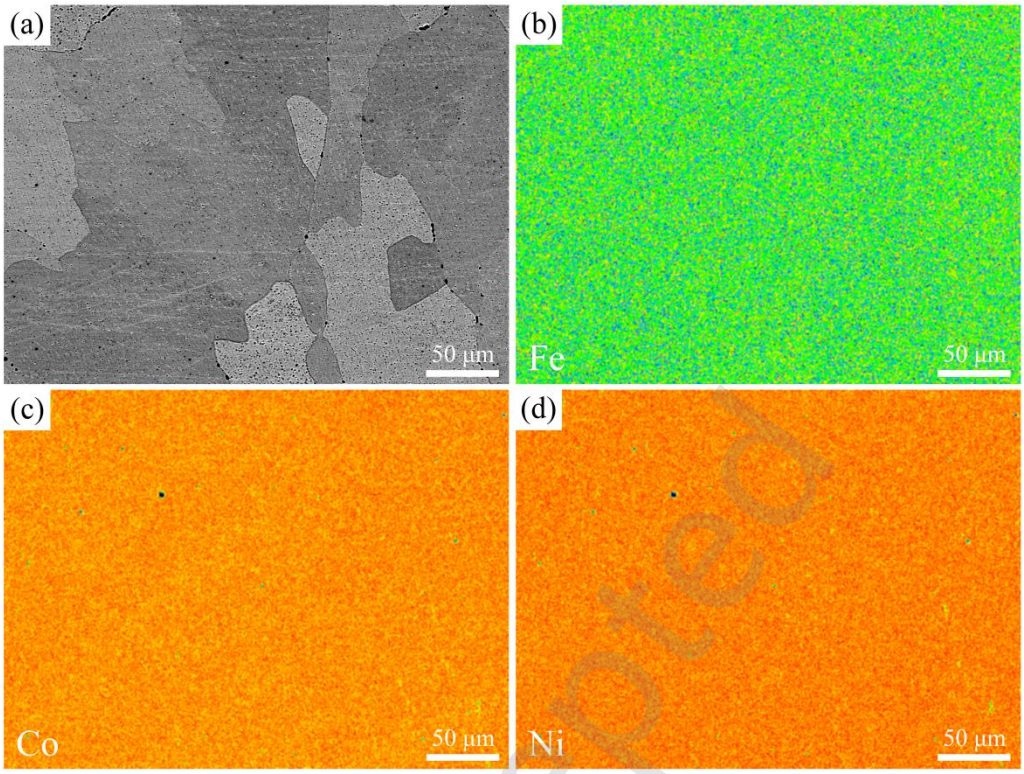


Figure S5 (a) SEM-BSE of the AC FeCoNi alloy; The corresponding EPMA elemental maps: (b) Fe; (c) Co; (d) Ni.

Just Accepted

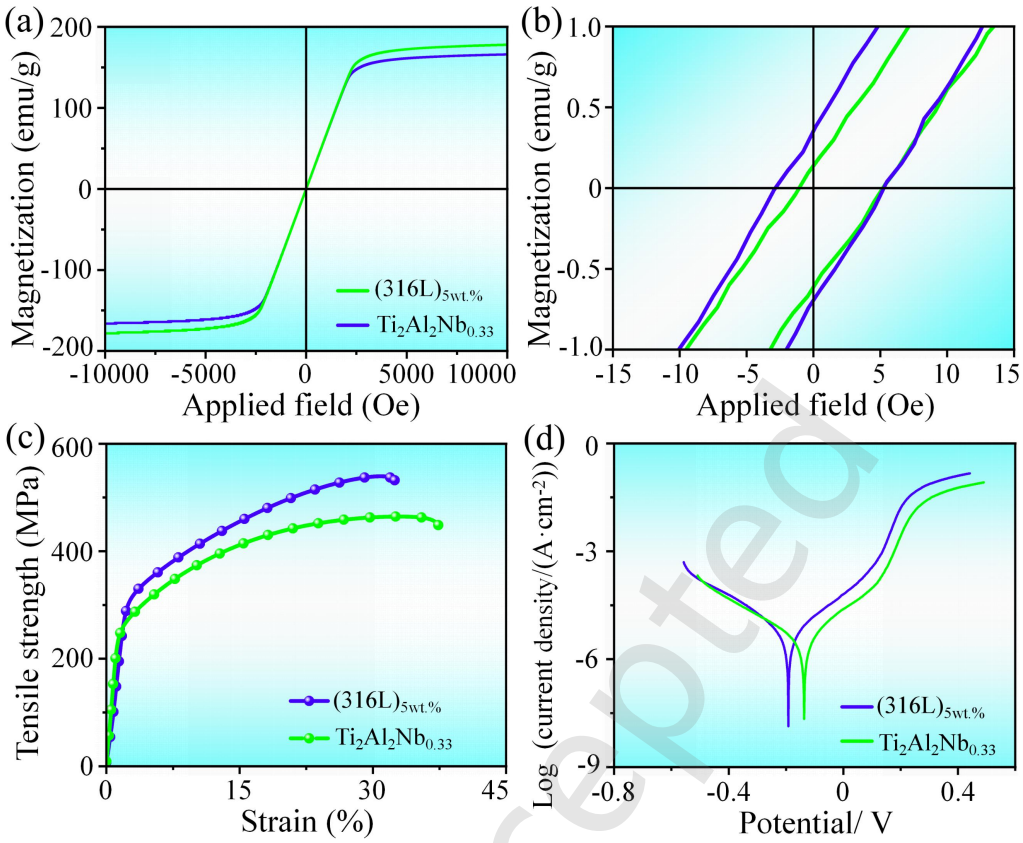


Figure S6 (a) Hysteresis loop at room temperature; (b) Enlargement of hysteresis near the origin; (c) Tensile engineering stress-strain curves at room temperature; (d) Dynamic potential polarization curves.

The origins of the strength, plasticity, and damage tolerance in both AC and AMed-AD alloys were further analyzed using SEM-BSE (**Fig. S7**). The AC alloy exhibits intergranular fracture accompanied by minimal plastic deformation, retaining a fully equiaxed grain structure (Figs. S7(a-c)). By comparison, grains within the AMed-AD alloy experience substantial tensile-axis deformation; both cellular and columnar grains become elongated, effectively hindering crack propagation under applied stress (Figs. S7(d-f)). This observation aligns with the superior tensile resistance of the AMed-AD alloy.

Just Accepted

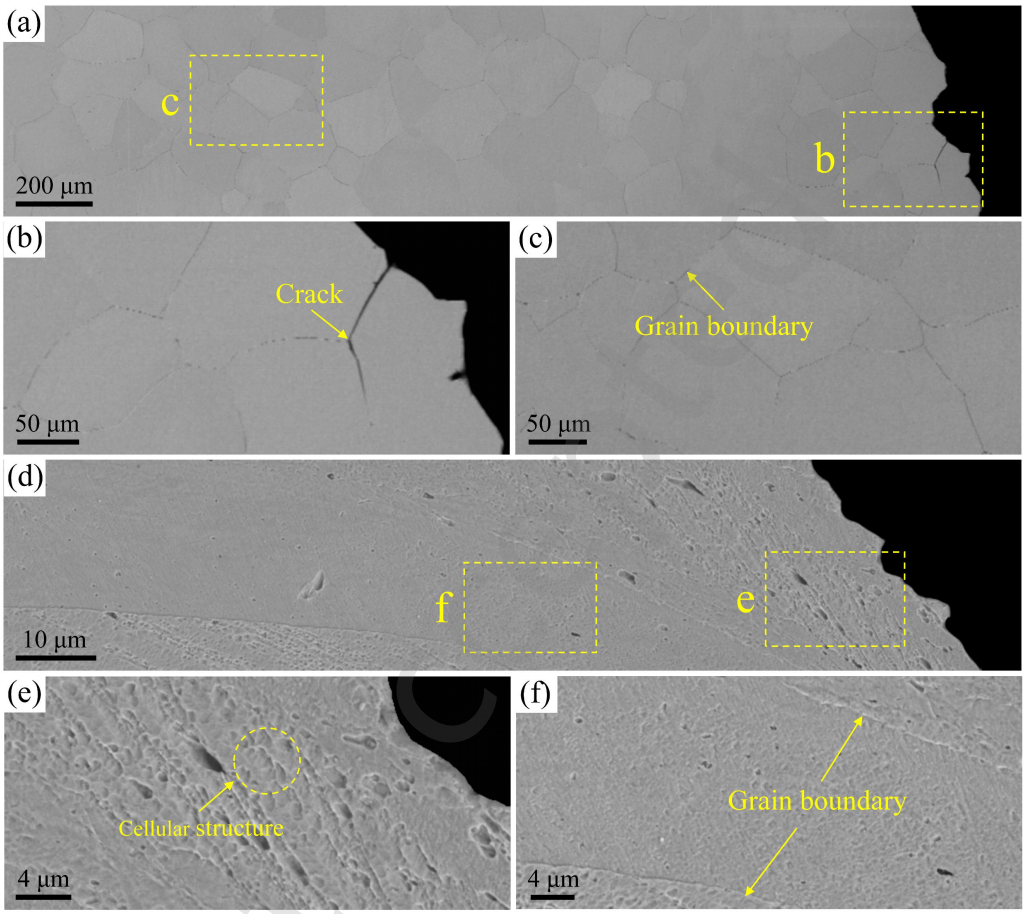


Figure S7 BSE-SEM images of the cross-sectional view at the regions close to the fracture surface for the alloy: (a) Crack propagation path of the AC alloy tensile sample; (b, c) Enlarged views of the local area in (a); (d) Crack propagation path of the AMed-AD tensile sample; (e, f) Enlarged views of the local area in (d).

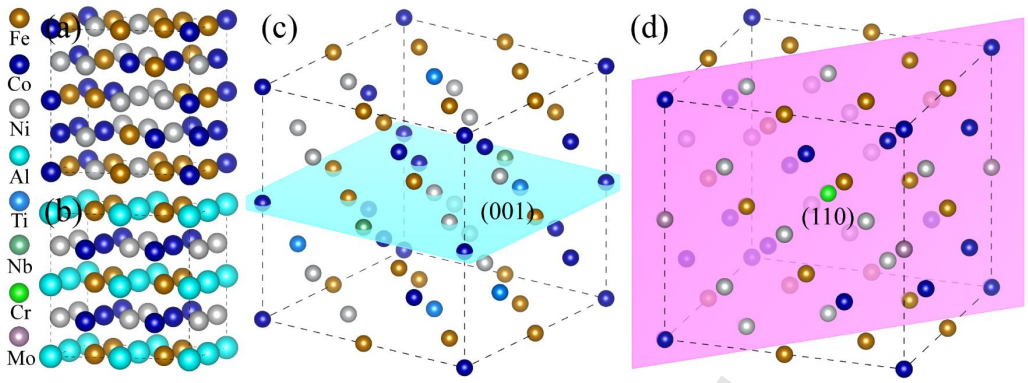


Figure S8 The geometry optimized unit structures: (a) γ-FeCoNi and (b) (Fe, Co, Ni)$_3$Al; The map of ELF slices located in geometry optimized structures: (a) Ti/Nb-doped γ-FeCoNi(001) and (b) Cr/Mo-doped γ-FeCoNi(110).

Just Accepted